Static and dynamic compressive and tensile response of highly stretchable polyurea

Xin Wang [a,e], Haibo Ji [b,c], Xue Li [b,c], Shengjie Sun [f], Qiancheng Zhang [a], V.P.W. Shim [d,e,*], Tian Jian Lu [b,c,**]

[a] *State Key Laboratory for Strength and Vibration of Mechanical Structures, Xi'an Jiaotong University, Xi'an 710049, China*
[b] *State Key Laboratory of Mechanics and Control of Mechanical Structures, Nanjing University of Aeronautics and Astronautics, Nanjing 210016, China*
[c] *MIIT Key Laboratory of Multifunctional Lightweight Materials and Structures, Nanjing University of Aeronautics and Astronautics, Nanjing 210016, China*
[d] *Key Laboratory of Impact and Safety Engineering (MOE), Ningbo University, Ningbo, Zhejiang 315211, China*
[e] *Impact Mechanics Laboratory, National University of Singapore, Singapore 117575, Singapore*
[f] *State Key Laboratory of Explosion Science and Technology, Beijing Institute of Technology, Beijing 100081, China*

ARTICLE INFO

ABSTRACT

The mechanical response of highly stretchable polyurea elastomer at various strain rates is investigated via experiments, theoretical analysis, and numerical modeling. Experiments encompassing quasi-static and dynamic (SHPB/SHTB - split Hopkinson pressure/tension bar) mechanical tests, as well as drop-weight impact tests, are undertaken to identify the nonlinear and rate-dependent relationship between tensile/compressive true stress and deformation of the polyurea studied. Subsequently, a compressible visco-hyperelastic constitutive model for the material is established based on the summation of Cauchy stress components. The proposed model yields good agreement with experimental data, as well as a better description of the tensile response at stretch rates of 10^3 s^{-1} than other models (e.g., the YSL2000 model (Yang et al., 2000) and the SYLL2004 model (Shim et al., 2004)). The model is implemented in the commercial finite element code Abaqus/Explicit via a user-defined material (VUMAT) subroutine. Homogenous deformation modes of polyurea, i.e., uniaxial compression and tension, are accurately captured, and non-uniform deformation of polyurea, corresponding to impact by a hemispherically-tipped drop weight, which induces both compression and tension, is also well described. Finally, it is demonstrated that the proposed model is able to characterize the dynamic response of other polyureas reported in literature. The present study is helpful for the design and development of blast and impact-resistant polyurea protective coatings.

1. Introduction

To mitigate blast and ballistic impact damage and improve the survivability of engineering structures, application of a polyurea coating to a wide range of substrates (e.g., metal, composite, concrete, masonry, etc.) has been increasingly adopted [1–6]. For instance, following the September 11 2001, attacks, the U.S. Air Force began spraying polyurea coatings on building walls to help maintain structural integrity during blast loading [7]. Such elastomeric coating can also decelerate explosion-generated fragments, thus protecting occupants within buildings. Polyurea elastomer is an environmentally-friendly copolymer, formed by condensation

polymerization of difunctional isocyanates (OCN-R-NCO) and difunctional amines (H$_2$N-R'-NH$_2$) precursors [8]. Fig. 1 shows a simplified single-chain molecular structure of polyurea, consisting of hard and soft domains [9], with interaction between adjacent molecular chains achieved via hydrogen bonds. The high water/corrosion/abrasion resistance and other favorable attributes of polyurea endow it with excellent stability in complex operating environments [10].

Based on the spray-cast fabrication technique, polyurea can be applied easily and rapidly. Maximizing its protective effects has become a topic of intense interest. Numerous experimental studies have examined the influence of several key factors, such as coating thickness,

---

coating location, and interfacial strength, in enhancing the blast/ballistic resistance of polyurea-coated structures; these have provided insights into underlying physical mechanisms [11–16]. However, conclusions drawn from experiments may be specific to particular substrate materials and loading modes adopted in individual studies. Blast and high-velocity ballistic tests are generally expensive and complex; hence, they can be supplemented and complemented by computational simulation to achieve efficient engineering designs involving polyurea coatings. To this end, establishment of simple yet effective constitutive models to characterize the mechanical behavior of polyurea, especially at high strain rates, is particularly useful.

In terms of earlier efforts, some theoretical models have been developed for the response of polyurea under blast and impact loading [17–24]. A rudimentary approach is to neglect rate sensitivity and assume that the mechanical behavior at a particular strain rate is sufficiently representative of the entire deformation history [25–27]. For instance, Xue et al. [26] established a six-parameter hyperelastic model calibrated using the tensile response at a strain rate of 10^4 s^{-1}, and simulated the penetration of steel-polyurea bilayer plates impacted by pointed and flat strikers. Chen et al. [27] formulated a two-parameter hyperelastic model based on the quasi-static tensile response of polyurea and used it to predict the deformation of polyurea-coated steel plates subjected to localized blast loading. A second approach is to employ rate-dependent elastoplastic stress-strain relationships [28–30], whereby Shi and his colleagues [31,32] adopted piecewise linear plasticity to calculate the blast resistance of concrete and steel plates incorporating a composite polyurea coating with a woven fiber mesh reinforcement. A third option is to modify classical hyperelastic models to encapsulate rate-dependence [21,33]; Raman et al. [33] and Mohotti et al. [21] proposed a modified hyperelastic model via a dynamic enhancement factor. Based on this, Mohotti et al. [34,35] simulated the dynamic response of polyurea-coated aluminum plates subjected to low/high-velocity projectile impact. A fourth perspective to incorporate rate sensitivity is to employ idealized hyperelastic and viscoelastic elements in parallel into a constitutive description [36]. Shim and Mohr [20] performed dynamic compressive tests and established a finite strain model encompassing two viscoelastic elements to describe polyurea, while Li and Lua [18] proposed a visco-hyperelastic theoretical description of the tensile behavior of polyurea at various strain rates.

However, there are still certain limitations in the application of these four methods. The first method, which ignores rate sensitivity, is the simplest but unable to model dynamic deformation over a wide range of strain rates [26]. The second approach, which assumes that polyurea behaves as an elastoplastic solid, cannot capture unloading of the material [37]. The third option essentially assumes that the true stress at an elevated high strain rate can be obtained by magnifying the quasi-static response through a fixed enhancement ratio. However, the stress enhancement ratio might not be constant for different stretches [21]. Consequently, appropriate selection of the dynamic stress enhancement ratio determines the prediction accuracy. The fourth approach is able to capture the mechanical response of polyurea at various strain rates, because the viscoelastic elements incorporated enable accommodation of the effect of strain rate history on the current stress [38,39]. Nevertheless, the degree of match with experimental results depends on the number of viscoelastic elements [40]. Consequently, a balance between the number of viscoelastic elements and preserving simplicity for the purpose of application, is a primary consideration.

The preceding review of recent work on modeling polyurea has identified several aspects which still need to be addressed: (i) previous investigations have focused primarily on either the compressive or tensile response of polyurea at different strain rates, and constitutive descriptions incorporating both compression and tension appear scant; (ii) generally, models are usually calibrated using experimental data from uniaxial loading tests, and the applicability of constitutive models developed to describe more complex loading situations involving both tension and compression has yet to be conclusively substantiated; (iii) applicability of constitutive models developed for a single specific polyurea, to describe other types of polyurea, remains to be demonstrated, since the properties of polyurea from different sources can vary significantly [41]. Thus, the current study employs experimental characterization, theoretical analysis, and numerical simulation to characterize the nonlinear compressive and tensile responses of polyurea elastomer at elevated strain rates, with particular focus on a highly stretchable polyurea that exhibits significant strength and ductility. The current model does not require the assumption of incompressibility in earlier idealizations [42], thus enabling the description of compressible visco-hyperelastic behavior, and its applicability to the polyurea studied, as well as nine other types of polyurea.
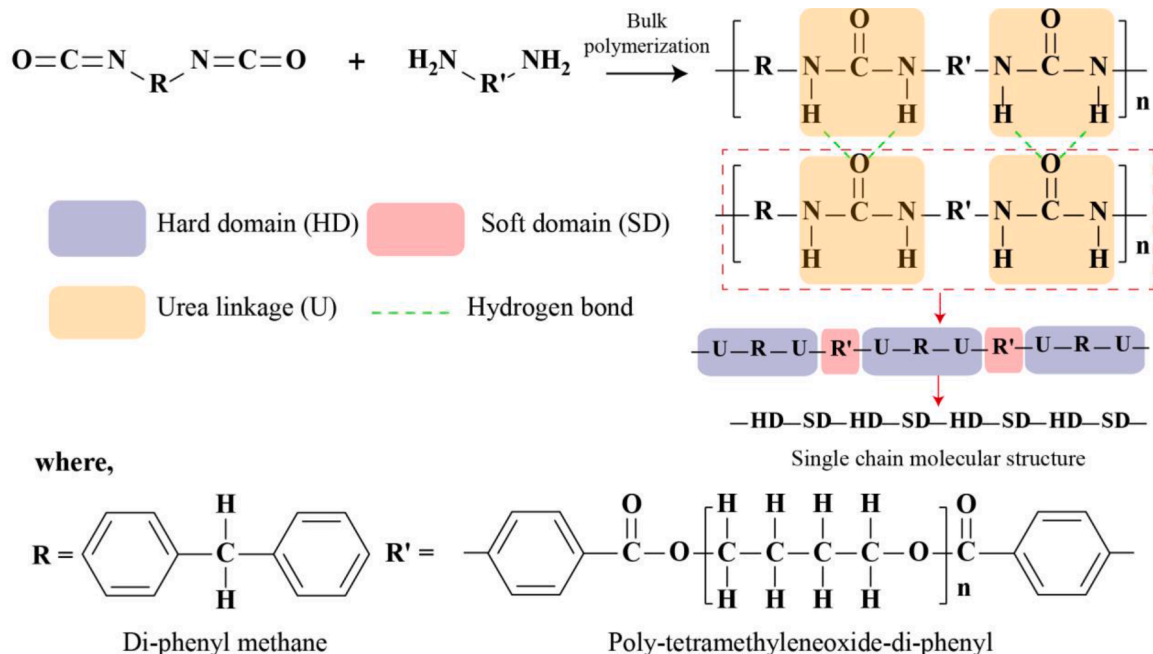

Fig. 1. Simplified schematic illustration of molecular-level structure of polyurea elastomer [9].

2. Material studied and experimental procedure

2.1. Material studied

The material of interest is Qtech-420 polyurea elastomer, with a density of 950 kg m^{-3}, supplied by Qingdao Shamu Advanced Material Co., Ltd., China. Before testing, the polyurea samples produced are maintained at room temperature for at least two weeks, as adequate curing time can enhance their mechanical properties. Experiments are then performed on polyurea samples in their pristine state, i.e., without any prior mechanical loading.

2.2. Quasi-static compression/tension tests

Quasi-static uniaxial tension and compression tests at an engineering strain rate (equal to the stretch rate) of 1×10^{-3} s^{-1} are conducted using a universal testing machine (SHIMADZU AGS-X). Following ISO 37:2017 (i.e., Rubber, vulcanized or thermoplastic - Determination of tensile stress-strain properties), dumbbell-shaped samples with a 33 mm gage length and 6 mm width are fabricated for tensile tests, as shown in Fig. 2a, with an optical extensometer employed to measure the deformation within the gage length. For compression tests, as shown in Fig. 2b, the dimensions of the cylindrical samples are similar to those used in SHPB tests. To ascertain consistency, tests corresponding to each mode of loading are done three times, and the average of the results is taken as representative of the material response. Prior to rupture, the polyurea samples exhibit excellent stretchability, elongating up to seven times their initial length (Fig. 3).

2.3. Dynamic compression/tension tests

Split Hopkinson pressure/tension bars (SHPB/SHTB) are employed for uniaxial tension and compression tests at high strain rates (~10^3 s^{-1}). The test samples are shown in Fig. 2c~d. For SHPB tests, the ASM

Handbook [43] recommends cylindrical specimens with a small length: diameter ratio (0.25~0.5) to facilitate rapid transmission of stress through the specimen and achievement of a constant stress state. To minimize inertial effects and frictional constraint at the specimen-bar interface, the specimen diameter should also be small relative to that of the bar [42]. For SHTB tests, dog-bone shaped samples with a 6 mm gage length and 3 mm width are adopted. The length:width ratio of the sample is at least 2:1, to achieve a uniaxial stress state within the gage length.

Fig. 4 shows the SHPB arrangement, comprising a gas chamber, striker, pulse shaper, input bar, output bar, damper, and data acquisition system. The striker, incident, and output bars are 16 mm in diameter and made of titanium alloy. From the work of Sarva et al. [44], a brass disk with a diameter of 6 mm and a thickness of 1 mm is utilized for pulse shaping to facilitate rapid attainment of equilibrium in specimens and reduce high-frequency noise in the input pulse. Based on well-established SHB analysis, the engineering strain rate $\dot{\varepsilon}_e$, engineering strain ε_e, and engineering stress σ_e in the sample are defined by [45]:

$$\dot{\varepsilon}_e(t) = -\frac{2c_b}{l_s}\varepsilon_r(t) \tag{1}$$

$$\varepsilon_e(t) = -\frac{2c_b}{l_s}\int_0^t \varepsilon_r(t)dt \tag{2}$$

$$\sigma_e(t) = \frac{A_b E_b}{A_s}\varepsilon_t(t) \tag{3}$$

where ε_i, ε_r and ε_t are the incident, reflected, and transmitted strains, respectively; l_s, A_s are the initial length and cross-sectional area of the sample, and A_b, E_b are the cross-sectional area and elastic modulus of the input/output bars; c_b is the elastic wave speed in the bar.

Fig. 5 shows the tensile SHTB counterpart, whereby the striker is tubular, the striker, input bar, and output bar are made of aluminum alloy, and the latter two have a diameter of 12 mm. In this instance, a
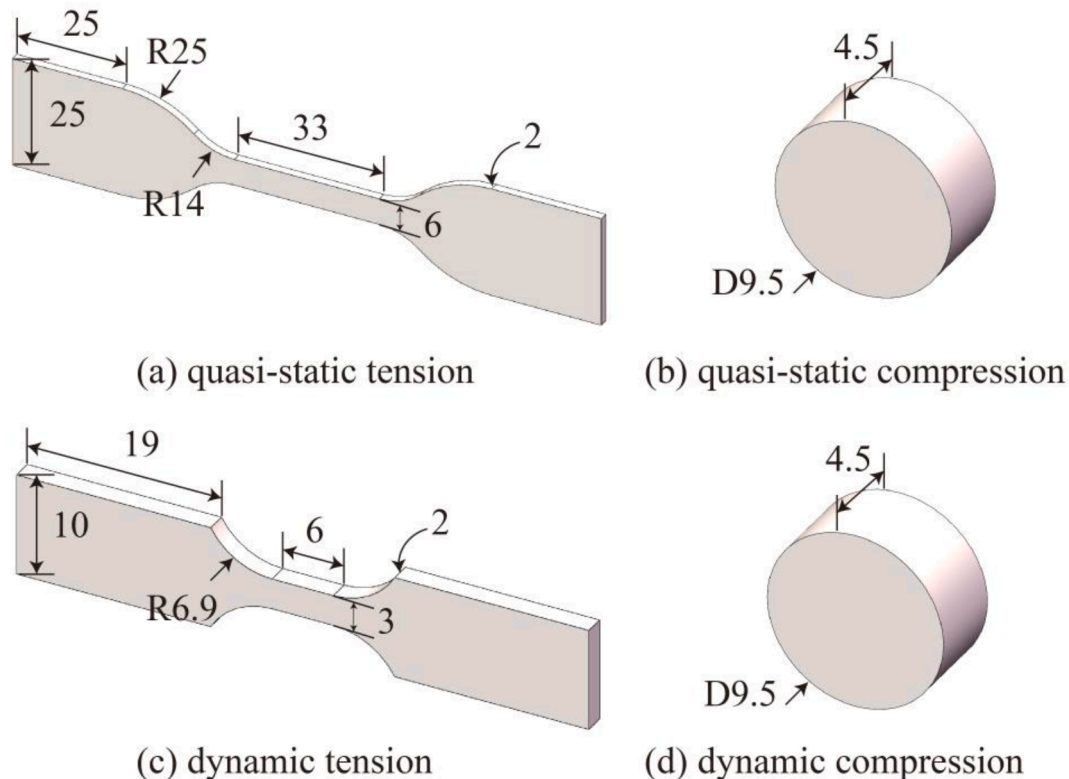

Fig. 2. Specimens for quasi-static and dynamic compression and tension tests (units: mm).

Fig. 3. Dumbbell-shaped sample under quasi-static uniaxial tension: (a) initial state and (b) highly stretched.
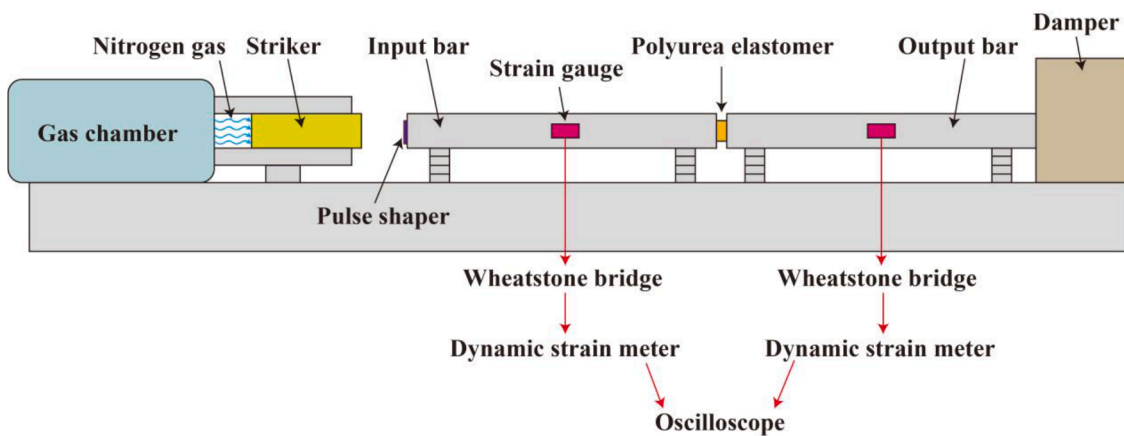

Fig. 4. Schematic diagram of split Hopkins pressure bar (SHPB) arrangement.
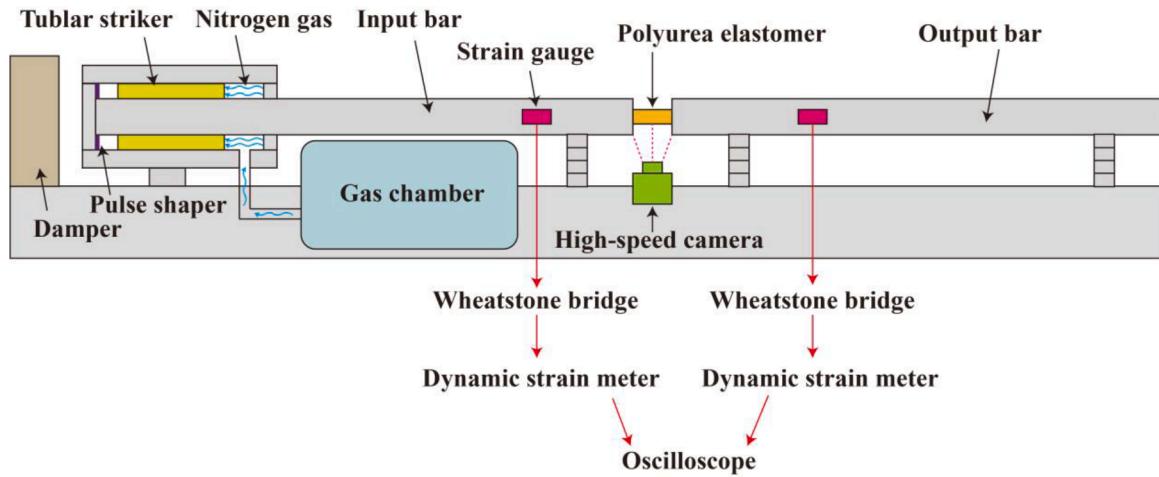
Fig. 5. Schematic diagram of split Hopkins tension bar (SHTB) arrangement.

high-speed camera is employed to obtain optical images of the specimen deformation. To enhance achievement of a uniform stress state, two consecutive pulse shapers are incorporated [46]. The specimen stress is also calculated using Eq. (3). Before each test, a speckle pattern is sprayed onto the surface of the specimen. A high-speed camera (FAST-CAM SA1.1, Photron) and a motion analysis software (TEMA 2D, IMAGESYSTEMS) are used to obtain and process optical images of the speckle positions, from which the strain within the gage length is determined. Compared with calculating the strain using Eq. (2), this method yields more accurate values of the strain within the gage length [47,48].

Fig. 6 shows typical strain gage signals associated with the first loading pulse, from SHPB and SHTB tests, respectively. With the aid of pulse shaping, the incident wave is approximately trapezoidal instead of rectangular, whereby the incident pulse rises to its peak more gradually to enhance stress equilibrium in samples [49]. The engineering strain rate is not perfectly constant but fluctuates somewhat as the specimen deforms (Fig. 7); this has also been observed in previous studies on polyurea [37,44,50]. As the fluctuations are not severe, the average strain rate is used in constitutive modeling. The results from dynamic tension/compression tests are summarized in Section 3.3.

2.4. Drop-weight impact tests

As shown in Fig. 8, drop-weight impact tests are conducted on circular samples with (i) base-supported and (ii) clamped-edge boundary conditions. The diameter D_s and thickness t_s of the samples are given in Table 1. A floor-standing impact system (INSTRON CEAST 9350) consisting of a hemispherical impactor, piezoelectric load cell, optical sensor, support plate, and specimen fixture, is used. The impactor is made of high-strength steel, and has a diameter of 16 mm, and the contact force between the impactor and sample is measured by the piezoelectric load cell with an operating range of $0 \sim 22$ kN. The optical sensor measures the impact velocity, and adjustment of the mass m_i and velocity v_i of the impactor enables prescription of the impact energy. Samples are mounted on the base plate or between the clamping fixture using a strong rapid-drying adhesive. Before testing, a thin layer of oil is applied to the impactor to reduce friction with the sample.

3. Constitutive modeling

3.1. Theoretical basis

With reference to traditional continuum analysis, a generic particle initially at some position $\mathbf{X}$ in a solid is displaced to position $\mathbf{x}$, resulting in a deformation gradient $\mathbf{F}$ defined by $\mathbf{F} = \partial \mathbf{x}/\partial \mathbf{X}$. The deformation can be expressed by the left Cauchy-Green deformation tensor $\mathbf{B} = \mathbf{F} \cdot \mathbf{F}^T$ or the right Cauchy-Green deformation tensor $\mathbf{C} = \mathbf{F}^T \cdot \mathbf{F}$, and the three invariants of $\mathbf{C}$ are defined as:
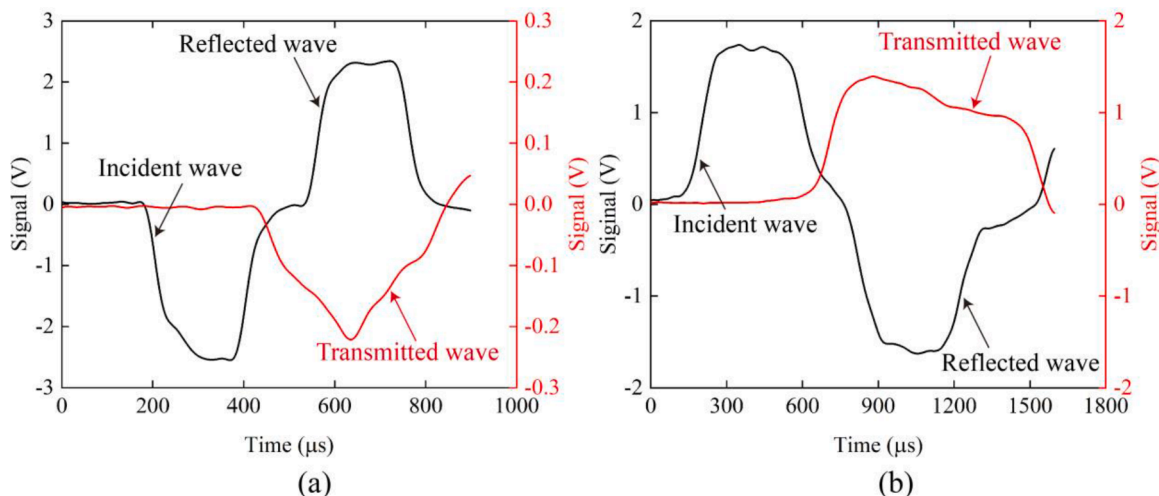

Fig. 6. Typical strain gage signals for the first loading pulse from (a) SHPB and (b) SHTB tests.
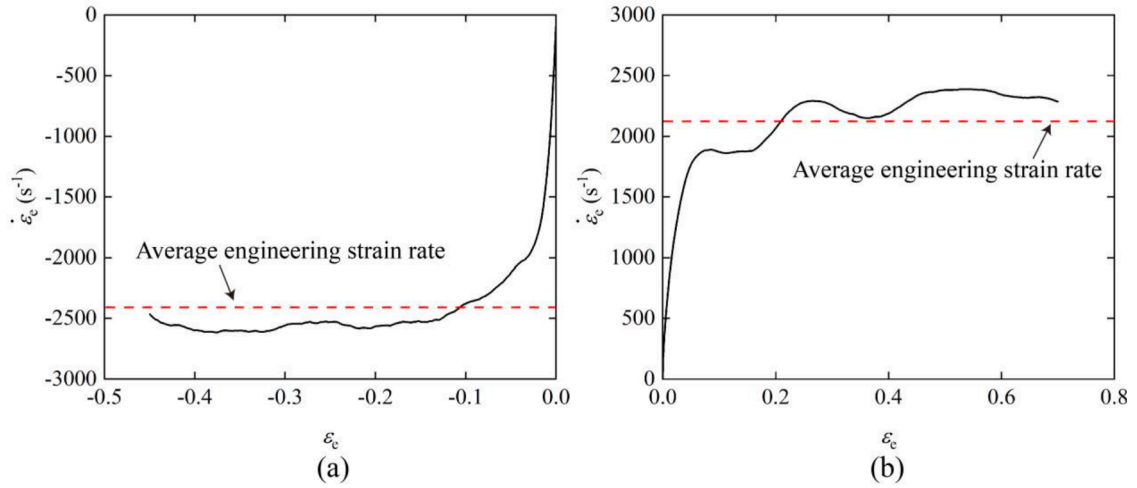
Fig. 7. Typical engineering strain rate histories from (a) SHPB and (b) SHTB tests.
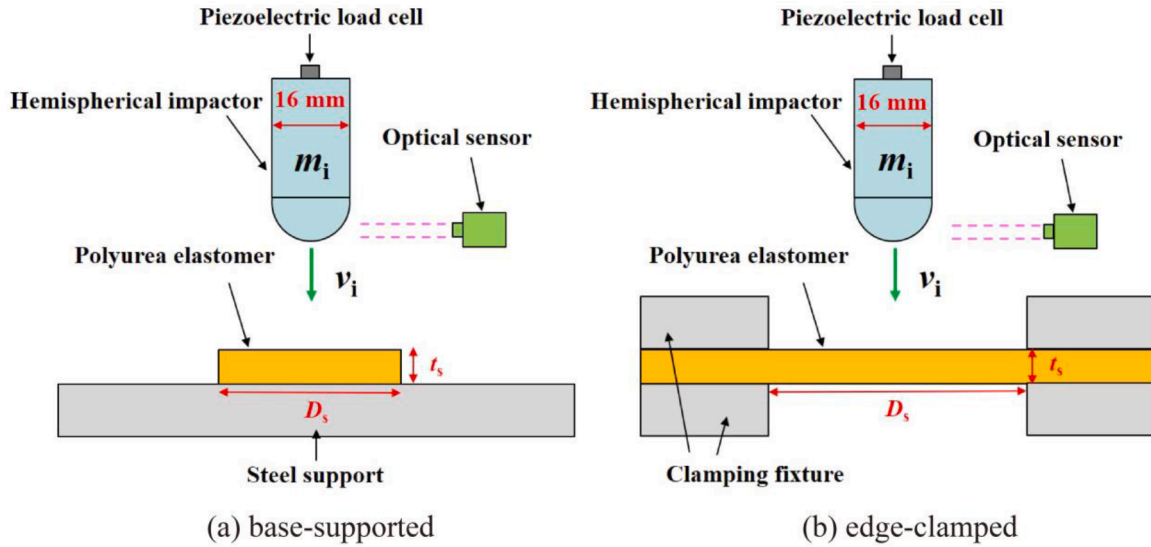

Fig. 8. Drop-weight impact tests on polyurea elastomer for (a) base-supported and (b) edge-clamped conditions.

Table 1
Details of drop-weight impact tests.

No.	Boundary condition	D_s (mm)	t_s (mm)	m_i (kg)	v_i (m/s)
1	Base-supported	24 ± 0.5	4 ± 0.2	2.277	1.74
2	Edge-clamped	60 ± 0.5	4 ± 0.2	2.277	1.86

$$I_1 = \mathrm{tr}(\mathbf{C}), I_2 = \frac{1}{2}\left[I_1^{\,2} - \mathrm{tr}(\mathbf{C}^2)\right], I_3 = \det(\mathbf{C}) \tag{4}$$

The Green-St.Venant strain tensor **E** is defined as:

$$\mathbf{E} = \frac{1}{2}(\mathbf{C} - \mathbf{I}) = \frac{1}{2}\left(\mathbf{F}^T \cdot \mathbf{F} - \mathbf{I}\right) \tag{5}$$

Consequently, the Green-St.Venant strain rate tensor is:

$$\dot{\mathbf{E}} = \frac{1}{2}\left(\dot{\mathbf{F}}^T \cdot \mathbf{F} + \dot{\mathbf{F}} \cdot \mathbf{F}^T\right) \tag{6}$$

To capture the rate-dependent response of polyurea, a commonly-used approach, first proposed by Green and Tobolsky [51], is adopted, whereby the total Cauchy stress can be decomposed into a time-independent hyperelastic component and a time-dependent viscoelastic component. As shown schematically in Fig. 9, parallel arrangement of the two components leads to their addition to obtain the Cauchy stress:

$$\boldsymbol{\sigma}^{vh} = \boldsymbol{\sigma}^{he} + \boldsymbol{\sigma}^{ve} \tag{7}$$

The superscripts he, ve, and vh denote hyperelasticity, viscoelasticity, and visco-hyperelasticity, respectively.

3.1.1. Hyperelasticity

For an isotropic, homogenous, and compressible hyperelastic solid, the Cauchy stress tensor $\boldsymbol{\sigma}^{he}$ can be expressed as [52]:

$$\boldsymbol{\sigma}^{he} = \frac{1}{J}\mathbf{F} \cdot \mathbf{T} \cdot \mathbf{F}^T \tag{8}$$

where J is the Jacobian of **F** which captures volumetric changes, and **T** is the second Piola-Kirchhoff stress tensor defined by [53]:

$$\mathbf{T} = \frac{\partial W}{\partial \mathbf{E}} = \frac{\partial W}{\partial I_1}\frac{\partial I_1}{\partial \mathbf{E}} + \frac{\partial W}{\partial I_2}\frac{\partial I_2}{\partial \mathbf{E}} + \frac{\partial W}{\partial J}\frac{\partial J}{\partial \mathbf{E}} \tag{9}$$
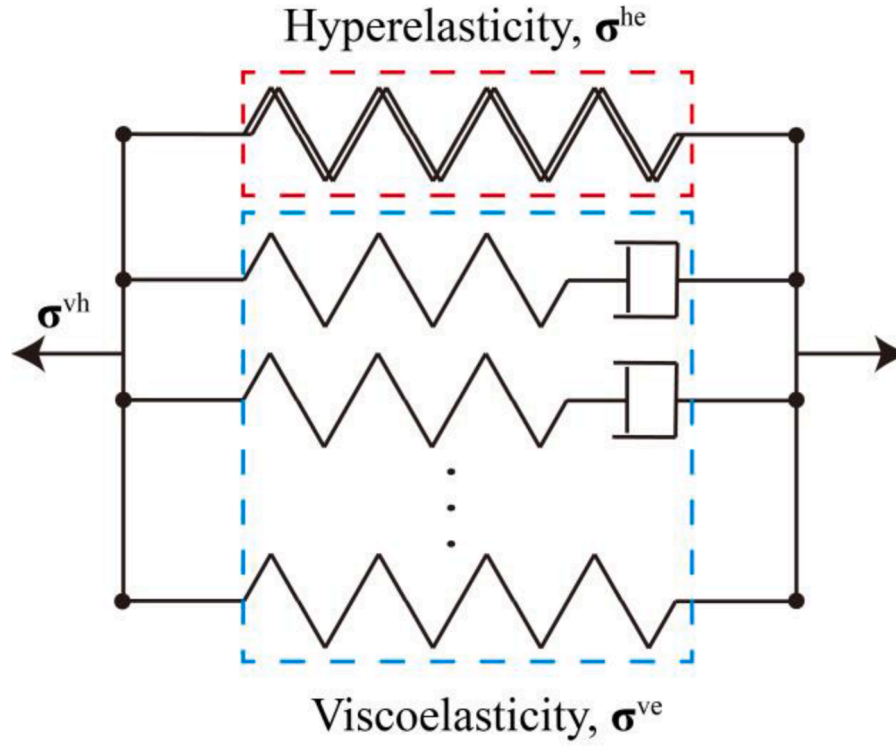
where

Fig. 9. Schematic illustration of the visco-hyperelastic model.

$$\frac{\partial I_1}{\partial \mathbf{E}} = \frac{\partial \mathrm{tr}(\mathbf{C})}{\partial \mathbf{E}} = \frac{\partial(3 + 2\mathrm{tr}(\mathbf{E}))}{\partial \mathbf{E}} = 2\mathbf{I}$$

$$\frac{\partial I_2}{\partial \mathbf{E}} = \frac{1}{2}\frac{\partial\left(\mathrm{tr}^2(\mathbf{C}) - \mathrm{tr}(\mathbf{C}^2)\right)}{\partial \mathbf{E}} = 2(I_1\mathbf{I} - \mathbf{C}) \tag{10}$$

$$\frac{\partial J}{\partial \mathbf{E}} = \left(\frac{1}{2}\frac{\partial\left(\mathbf{F}^{\mathrm{T}}\cdot\mathbf{F} - \mathbf{I}\right)}{\partial J}\right)^{-1} = \left(\frac{1}{2}\frac{1}{J}\frac{\partial J\mathbf{F}^{\mathrm{T}}}{\partial J}\cdot\mathbf{F} + \frac{1}{2}\frac{1}{J}\mathbf{F}^{\mathrm{T}}\cdot\frac{\partial J\mathbf{F}}{\partial J}\right)^{-1} = J\mathbf{C}^{-1}$$

Substitution of Eqs. (9) and (10) into Eq. (8) yields:

$$\boldsymbol{\sigma}^{\mathrm{he}} = \frac{2}{J}\left(\frac{\partial W}{\partial I_1} + I_1\frac{\partial W}{\partial I_2}\right)\mathbf{B} - \frac{2}{J}\frac{\partial W}{\partial I_2}\mathbf{B}^2 + \frac{\partial W}{\partial J}\mathbf{I} \tag{11}$$

where W is the strain energy function and $\mathbf{I}$ is the unit tensor. In general, the definition of W determines the form and appropriateness of the model. With reference to Boyce and Arruda [54], the strain energy function can be split into isochoric and volumetric contributions:

$$W = W_{\mathrm{iso}} + W_{\mathrm{vol}} \tag{12}$$

The isochoric part W_{iso} can usually be viewed from two perspectives - statistical mechanics and continuum mechanics. Rivlin [55] developed a continuum mechanics-based model for W_{iso} in terms of functions of I_1, I_2 and J, namely:

$$W_{\mathrm{iso}} = \sum_{i,j=0}^{\infty} A_{ij}\left(J^{-\frac{2}{3}}I_1 - 3\right)^{i}\left(J^{-\frac{4}{3}}I_2 - 3\right)^{j} \tag{13}$$

where A_{ij} are undetermined coefficients. Arruda and Boyce [54] also commented that such a phenomenological model is equivalent to a microstructure-based statistical mechanics model when high-order I_1 terms are introduced. A quadratic function of J is adopted to model the volumetric component W_{vol}, as in [56]:

$$W_{\mathrm{vol}} = D(J - 1)^2 \tag{14}$$

where D is a material constant, defined in [57]:

$$D = \frac{K}{2} = \frac{E}{6(1 - 2\mu)} \tag{15}$$

and K is the bulk modulus, E the Young's modulus, and μ the Poisson's ratio. For a compressible hyperelastic solid, substitution of Eqs. (13) and (14) into Eq. (12) leads to a general expression for the strain energy potential:

$$W = \sum_{i,j=0}^{\infty} A_{ij}\left(J^{-\frac{2}{3}}I_1 - 3\right)^{i}\left(J^{-\frac{4}{3}}I_2 - 3\right)^{j} + D(J - 1)^2 \tag{16}$$

With the objective of limiting the number of parameters, Shim et al. [38] found that a three-term form for the isochoric component W_{iso} is sufficient to model both the tensile and compressive responses of rubber. Therefore, the strain energy function W of Eq. (16) can be reduced to:

$$W = A_1\left(J^{-\frac{2}{3}}I_1 - 3\right) + A_2\left(J^{-\frac{4}{3}}I_2 - 3\right) + A_3\left(J^{-\frac{2}{3}}I_1 - 3\right)\left(J^{-\frac{4}{3}}I_2 - 3\right) + D(J - 1)^2 \tag{17}$$

However, when describing large deformations, a simple form of the strain energy potential may lead to errors [54]. Yeoh [58,59] noted that introduction of higher-order I_1 terms facilitates modeling of moderate to large deformations. The present study proposes incorporation of an exponential term involving I_1, leading to:

$$W = A_1\left(J^{-\frac{2}{3}}I_1 - 3\right) + A_2\left(J^{-\frac{4}{3}}I_2 - 3\right) + A_3\left(J^{-\frac{2}{3}}I_1 - 3\right)\left(J^{-\frac{4}{3}}I_2 - 3\right) + \frac{A_4}{A_5}\left(1 - e^{-A_5\left(J^{-\frac{2}{3}}I_1 - 3\right)}\right) + D(J - 1)^2 \tag{18}$$

As with other high-order I_1 models (e.g., the Gent model [60]), the exponential term involving I_1 in Eq. (18) can be expanded via a Taylor series to yield the following:

$$\frac{A_4}{A_5}\left(1 - e^{-A_5\left(J^{-\frac{2}{3}}I_1 - 3\right)}\right) = \frac{A_4}{A_5}\sum_{i=1}^{\infty}\frac{(-A_5)^{i}\left(J^{-\frac{2}{3}}I_1 - 3\right)^{i}}{i!} \tag{19}$$

Finally, combination of Eqs. (11) and (18) yields the Cauchy stress for a compressible hyperelastic solid:

$$\boldsymbol{\sigma}^{\mathrm{he}} = -2\left(\left(A_2 + A_3\left(J^{-\frac{2}{3}}I_1 - 3\right)\right)J^{-\frac{7}{3}}\right)\mathbf{B}^2$$

$$+2\left(\left(A_1 + A_4 e^{-A_5\left(J^{-\frac{2}{3}}I_1 - 3\right)}\right)J^{-\frac{5}{3}} + \left(A_2 + A_3\left(J^{-\frac{2}{3}}I_1 - 3\right)\right)J^{-\frac{7}{3}}I_1 + A_3\left(J^{-\frac{4}{3}}I_2 - 3\right)J^{-\frac{5}{3}}\right)\mathbf{B}$$

$$+\left(2D(J-1) - \frac{2}{3}\left(A_1 + A_4 e^{-A_5\left(J^{-\frac{2}{3}}I_1 - 3\right)}\right)J^{-\frac{5}{3}}I_1 - \frac{4}{3}\left(A_2 + A_3\left(J^{-\frac{2}{3}}I_1 - 3\right)\right)J^{-\frac{7}{3}}I_2 - \frac{2}{3}A_3\left(J^{-\frac{4}{3}}I_2 - 3\right)J^{-\frac{5}{3}}\right)\mathbf{I} \tag{20}$$

3.1.2. Viscoelasticity

A primary feature of a viscoelastic solid is the fading memory effect, which implies that the present stress depends strongly on strain/strain rate history [61]. Based on linear viscoelasticity [52], the Cauchy stress tensor $\boldsymbol{\sigma}^{\mathrm{ve}}$ for an isotropic, homogenous, and compressible viscoelastic solid can be expressed as:

$$\boldsymbol{\sigma}^{\mathrm{ve}} = \int_{-\infty}^{t} \boldsymbol{\Psi}(t-\tau) : \frac{d\boldsymbol{\varepsilon}^{\mathrm{ve}}}{d\tau} d\tau \tag{21}$$

where $\boldsymbol{\varepsilon}^{\mathrm{ve}}$ is the viscoelastic Cauchy strain and $\boldsymbol{\Psi}$ is a fourth-order relaxation modulus tensor. As with previous analysis [17], the relaxation modulus tensor can be divided into two components – deviatoric and dilatational:

$$\boldsymbol{\Psi}(t) = \left[\Gamma(t)\delta_{\mathrm{ij}}\delta_{\mathrm{pq}} + G(t)\left(\delta_{\mathrm{ip}}\delta_{\mathrm{jq}} + \delta_{\mathrm{iq}}\delta_{\mathrm{jp}}\right)\right]\mathbf{e_i} \otimes \mathbf{e_j} \otimes \mathbf{e_p} \otimes \mathbf{e_q} \tag{22}$$

where $\Gamma(t)$ and $G(t)$ are the Lamé parameters and δ_{ij} is the Kronecker delta. Correspondingly, the Cauchy strain $\boldsymbol{\varepsilon}^{\mathrm{ve}}$ can be separated into the deviatoric strain $\mathbf{s}^{\mathrm{ve}}$ and the volumetric strain ε_{v}, as:

$$\boldsymbol{\varepsilon}^{\mathrm{ve}} = \frac{1}{3}\mathrm{tr}(\boldsymbol{\varepsilon}^{\mathrm{ve}})\mathbf{I} + \mathbf{s}^{\mathrm{ve}} = \frac{1}{3}\varepsilon_{\mathrm{v}}\mathbf{I} + \mathbf{s}^{\mathrm{ve}} \tag{23}$$

Combining Eqs. (21) ~ (23) yields:

$$\boldsymbol{\sigma}^{\mathrm{ve}} = \int_{-\infty}^{t}\left[\Gamma(t-\tau)\dot{\varepsilon}_{\mathrm{v}}\mathbf{I} + 2G(t-\tau)\dot{\boldsymbol{\varepsilon}}^{\mathrm{ve}}\right]d\tau \tag{24}$$

where $\dot{\varepsilon}_{\mathrm{v}}$ is the volumetric strain rate. From the Lamé parameters, the bulk modulus $K(t)$ can be expressed as:

$$K(t) = \Gamma(t) + \frac{2}{3}G(t) \tag{25}$$

Hence, Eq. (24) can be rewritten as:

$$\boldsymbol{\sigma}^{\mathrm{ve}} = \int_{-\infty}^{t}\left[K(t-\tau)\dot{\varepsilon}_{\mathrm{v}}\mathbf{I} + 2G(t-\tau)\dot{\mathbf{s}}^{\mathrm{ve}}\right]d\tau \tag{26}$$

where $\dot{\mathbf{s}}^{\mathrm{ve}}$ is the deviatoric Cauchy strain rate. As with the well-known Maxwell model [52], the bulk modulus $K(t-\tau)$ and shear modulus $G(t-\tau)$ can be expressed in terms of a Prony series.

$$K(t-\tau) = K_\infty + \sum_{\mathrm{i}=1}^{N} K_{\mathrm{i}} e^{-\frac{t-\tau}{\theta_{\mathrm{i}}}} \tag{27}$$

$$G(t-\tau) = G_\infty + \sum_{\mathrm{i}=1}^{N} G_{\mathrm{i}} e^{-\frac{t-\tau}{\theta_{\mathrm{i}}}} \tag{28}$$

Substitution of Eqs. (27) and (28) into Eq. (26) yields the Cauchy stress for a linear viscoelastic solid:

$$\boldsymbol{\sigma}^{\mathrm{ve}} = \int_{-\infty}^{t}\left(K_\infty + \sum_{\mathrm{i}=1}^{N} K_{\mathrm{i}} e^{-\frac{t-\tau}{\theta_{\mathrm{i}}}}\right)\dot{\varepsilon}_{\mathrm{v}}\mathbf{I}d\tau + \int_{-\infty}^{t} 2\left(G_\infty + \sum_{\mathrm{i}=1}^{N} G_{\mathrm{i}} e^{-\frac{t-\tau}{\theta_{\mathrm{i}}}}\right)\dot{\mathbf{s}}^{\mathrm{ve}}d\tau$$

$$= \left(K_\infty \varepsilon_{\mathrm{v}} + \sum_{\mathrm{i}=1}^{N} K_{\mathrm{i}} \int_{-\infty}^{t} e^{-\frac{t-\tau}{\theta_{\mathrm{i}}}}\dot{\varepsilon}_{\mathrm{v}}d\tau\right)\mathbf{I} + 2\left(G_\infty \mathbf{s}^{\mathrm{ve}} + \sum_{\mathrm{i}=1}^{N} G_{\mathrm{i}} \int_{-\infty}^{t} e^{-\frac{t-\tau}{\theta_{\mathrm{i}}}}\dot{\mathbf{s}}^{\mathrm{ve}}d\tau\right) \tag{29}$$

where θ_{i} are the relaxation time constants and N is the number of constants. Note that the bulk modulus parameters K_∞ and K_{i} can be calculated using the shear modulus parameters (G_∞ and G_{i}) and the Poisson's ratio (μ):

$$K_\infty = \frac{2(1+\mu)}{3(1-2\mu)}G_\infty \tag{30}$$

$$K_{\mathrm{i}} = \frac{2(1+\mu)}{3(1-2\mu)}G_{\mathrm{i}} \tag{31}$$

Therefore, for linear viscoelasticity, the number of independent model parameters in Eq. (29) is $3 \times N$. Selection of the number of relaxation time constants N affects the results predicted by the model, and should be carefully considered [38]. Generally, the values and number of relaxation times θ_{i} are associated with many factors [62], such as load magnitude, loading speed, temperature, friction, wear, aging, etc. To consider the influence of such factors, Pouriayevali et al. [39] and Khajehsaeid et al. [63] expressed the relaxation time as strain-dependent and strain-rate-dependent functions, respectively. Yang et al. [40] suggested that the mechanical response of a polymeric solid over a range of strain rates (up to $10^3 \mathrm{~s}^{-1}$) measured using SHPB/SHTB devices can be described by a single relaxation time. In this work, the strain rate range of concern is $10^3 \sim 10^4 \mathrm{~s}^{-1}$, which is usually experienced by polyurea elastomer during explosive and high-velocity impact loading [1,38,47,48]. To minimize the model parameters, only one relaxation time ($N = 1$) is adopted in Eq. (29). (With regard to the influence of increasing the number of relaxation time constants in the model on its predictions, a second Prony-series term was incorporated, resulting in two additional constants. The results showed a negligible improvement in the goodness-of-fit value (R^2) between the experimental and predicted results by only 0.002%, indicating that the model with one Prony-series term is adequate in describing the dynamic response of the polyurea elastomers examined.) If the model is required to predict accurately the mechanical response over a larger strain rate range, increasing the number of relaxation times N would facilitate this. Assuming that the effect of loading history ($-\infty < \tau < 0$) on the Cauchy stress is neglected, the final expression for the viscoelastic stress is:

$$\boldsymbol{\sigma}^{\mathrm{ve}} = \frac{2(1+\mu)}{3(1-2\mu)}\left(G_\infty \varepsilon_{\mathrm{v}} + G_1 \int_0^t e^{-\frac{t-\tau}{\theta_1}}\dot{\varepsilon}_{\mathrm{v}}d\tau\right)\mathbf{I} + 2\left(G_\infty \mathbf{s}^{\mathrm{ve}} + G_1 \int_0^t e^{-\frac{t-\tau}{\theta_1}}\dot{\mathbf{s}}^{\mathrm{ve}}d\tau\right) \tag{32}$$

3.1.3. Visco-hyperelasticity

As shown in Fig. 9, the total Cauchy stress for a visco-hyperelastic solid can be decomposed into a time-independent hyperelastic component and a time-dependent viscoelastic component. Therefore, substitution of Eqs. (20) and (32) into Eq. (7) results in a general expression for the three-dimensional visco-hyperelastic constitutive model:

$$\mathbf{F} = \begin{bmatrix} \lambda & 0 & 0 \\ 0 & \lambda^{-\mu} & 0 \\ 0 & 0 & \lambda^{-\mu} \end{bmatrix}, \mathbf{B} = \mathbf{F} \cdot \mathbf{F}^{\mathrm{T}} = \begin{bmatrix} \lambda^2 & 0 & 0 \\ 0 & \lambda^{-2\mu} & 0 \\ 0 & 0 & \lambda^{-2\mu} \end{bmatrix}, \mathbf{C} = \mathbf{F}^{\mathrm{T}} \cdot \mathbf{F} = \begin{bmatrix} \lambda^2 & 0 & 0 \\ 0 & \lambda^{-2\mu} & 0 \\ 0 & 0 & \lambda^{-2\mu} \end{bmatrix} \tag{34}$$

The three invariants of $\mathbf{C}$ are:

$$
\begin{aligned}
\boldsymbol{\sigma}^{\mathrm{vh}} &= \boldsymbol{\sigma}^{\mathrm{he}} + \boldsymbol{\sigma}^{\mathrm{ve}} \\
&= -2\left(\left(A_2 + A_3\left(J^{-\frac{2}{3}}I_1 - 3\right)\right)J^{-\frac{7}{3}}\right)\mathbf{B}^2 \\
&\quad + 2\left(\left(A_1 + A_4 e^{-A_5\left(J^{-\frac{2}{3}}I_1 - 3\right)}\right)J^{-\frac{5}{3}} + \left(A_2 + A_3\left(J^{-\frac{2}{3}}I_1 - 3\right)\right)J^{-\frac{7}{3}}I_1 + A_3\left(J^{-\frac{4}{3}}I_2 - 3\right)J^{-\frac{5}{3}}\right)\mathbf{B} \\
&\quad + \left(2D(J-1) - \frac{2}{3}\left(A_1 + A_4 e^{-A_5\left(J^{-\frac{2}{3}}I_1 - 3\right)}\right)J^{-\frac{5}{3}}I_1 - \frac{4}{3}\left(A_2 + A_3\left(J^{-\frac{2}{3}}I_1 - 3\right)\right)J^{-\frac{7}{3}}I_2 - \frac{2}{3}A_3\left(J^{-\frac{4}{3}}I_2 - 3\right)J^{-\frac{5}{3}}\right)\mathbf{I} \\
&\quad + \frac{2(1+\mu)}{3(1-2\mu)}\left(G_\infty \varepsilon_v + G_1 \int_0^t e^{-\frac{t-\tau}{\theta_1}}\dot{\varepsilon}_v d\tau\right)\mathbf{I} + 2\left(G_\infty \mathbf{s}^{\mathrm{ve}} + G_1 \int_0^t e^{-\frac{t-\tau}{\theta_1}}\dot{\mathbf{s}}^{\mathrm{ve}} d\tau\right)
\end{aligned}
\tag{33}
$$

where $A_1, A_2, A_3, A_4, A_5, G_\infty, G_1$ and θ_1 are constants to be determined.

3.2. Parameter evaluation

In this work, polyurea elastomer is modeled as a nearly incompressible solid with a Poisson's ratio of 0.485, similar to that in a previous effort [17], as a small degree of compressibility is required for finite element (FE) implementation – e.g., via the user-defined material subroutine in Hohenberger et al. [57]. The one-dimensional parameter

$$I_1 = \mathrm{tr}(\mathbf{C}) = 2\lambda^{-2\mu} + \lambda^2, I_2 = \frac{1}{2}\left[I_1{}^2 - \mathrm{tr}\left(\mathbf{C}^2\right)\right] = \lambda^{-4\mu} + 2\lambda^{2-2\mu}, I_3 = \det(\mathbf{C}) = \lambda^{2-4\mu} \tag{35}$$

Substitution of Eqs. (34) and (35) into Eq. (20), together with the uniaxial loading condition ($\sigma_{22} = \sigma_{33} = 0$) and the assumption of compressibility ($\mu = 0.485$), results in a true stress-stretch relationship in the loading direction:

$$
\begin{aligned}
\sigma_{11} &= \sigma_{11}^{\mathrm{he}} - \sigma_{22}^{\mathrm{he}} \\
&= 2\left(\frac{A_2}{\lambda^{2.01}} + \frac{A_1 + A_4 e^{-A_5\left(-3 + \frac{2}{\lambda^{0.99}} + \lambda^{1.98}\right)}}{\lambda^{1.02}}\right)\left(-1 + \lambda^{2.97}\right) + \frac{6A_3\left(-\lambda^{3.03} + \lambda^{4.02} + \lambda^{5.01} - \lambda^{6.99} - \lambda^{7.98} + \lambda^{8.97}\right)}{\lambda^{6.03}}
\end{aligned}
\tag{36}
$$

calibration process adopted comprises two steps: (i) the hyperelastic model parameters $A_1 \sim A_5$ are identified through fitting quasi-static test data to Eq. (36); (ii) the viscoelastic model parameters G_1, G_∞ and θ_1 are obtained through fitting high-rate test data to Eq. (40). Data fitting is effected using the commercial software Wolfman Mathematica v12.0, with optimal model parameters obtained using the built-in Levenberg-Marquardt algorithm. A one-dimensional version of the theoretical basis for the model is now briefly introduced.

Consider quasi-static uniaxial loading of an isotropic compressible sample; the stretch in the loading direction is denoted by λ, and thus the three principal stretches are $\lambda_1 = \lambda$ and $\lambda_2 = \lambda_3 = \lambda^{-\mu}$. The resulting deformation gradient $\mathbf{F}$ and the left/right Cauchy-Green deformation tensor $\mathbf{B}$, $\mathbf{C}$ are:

Consider next, uniaxial loading at a high strain rate. The stretch in the loading direction is also denoted by λ; thereby, the three principal stretches are again $\lambda_1 = \lambda$ and $\lambda_2 = \lambda_3 = \lambda^{-\mu}$, and the Cauchy strain tensor $\boldsymbol{\varepsilon}^{\mathrm{ve}}$ can thence be defined as [53]:

$$\boldsymbol{\varepsilon}^{\mathrm{ve}} = \begin{bmatrix} \lambda - 1 & 0 & 0 \\ 0 & \lambda^{-\mu} - 1 & 0 \\ 0 & 0 & \lambda^{-\mu} - 1 \end{bmatrix} \tag{37}$$

Based on strain decomposition according to Eq. (23), the deviatoric Cauchy strain tensor $\mathbf{s}^{\mathrm{ve}}$ is:
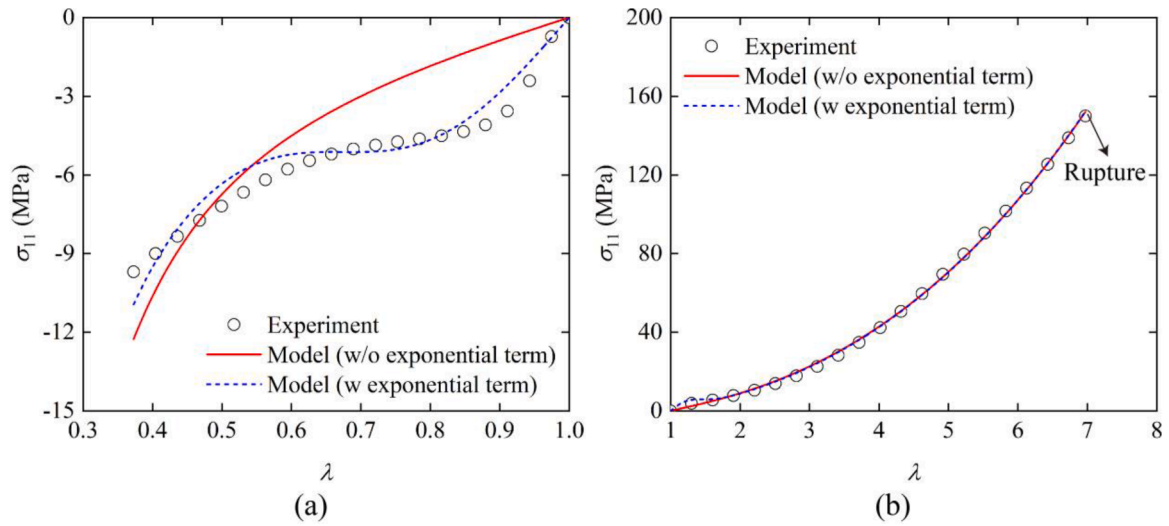
Fig. 10. Comparison between experimental and theoretical results for polyurea elastomer under quasi-static loading (0.001 s^{-1}): (a) compression and (b) tension.
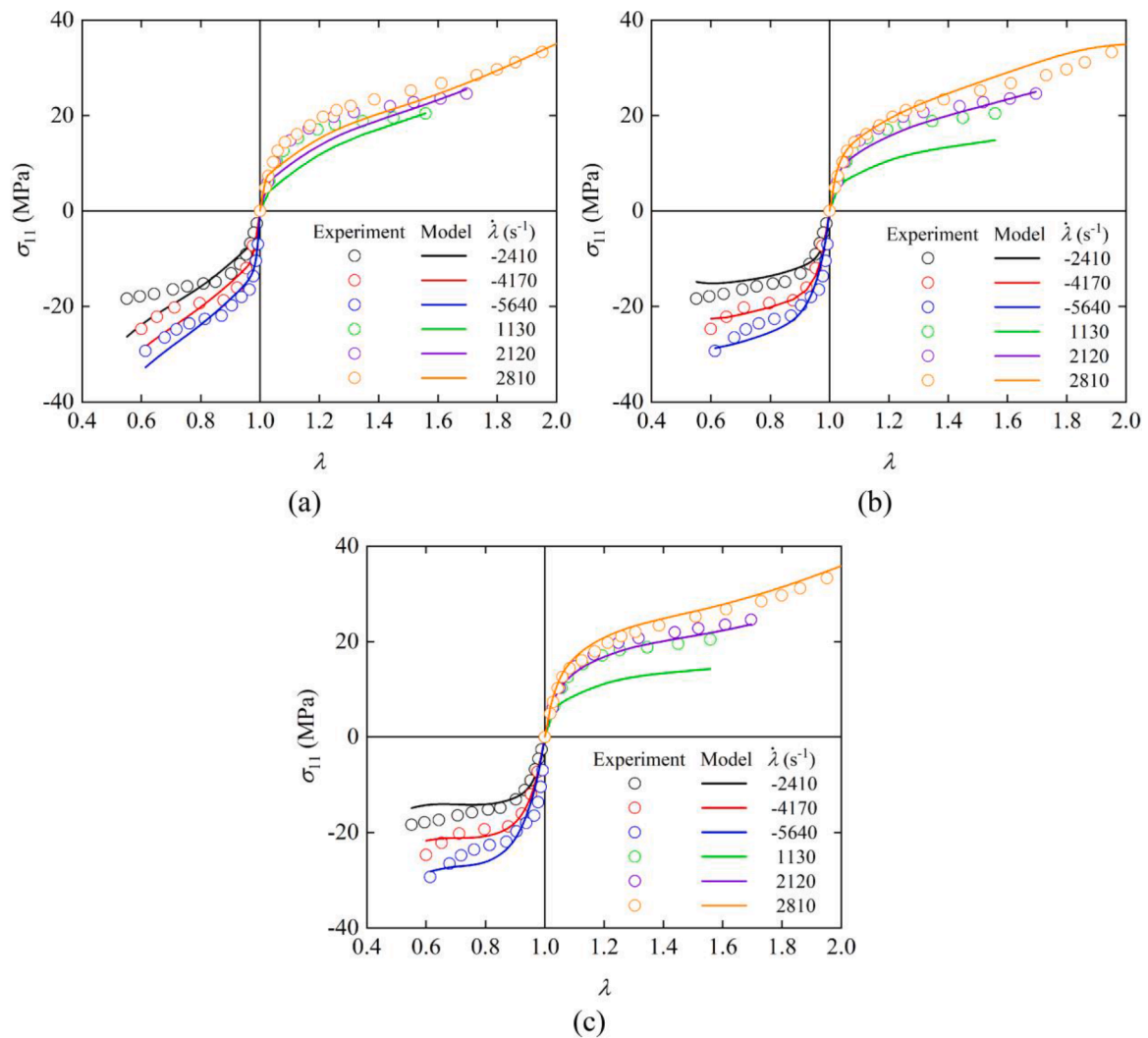

Fig. 11. Response of polyurea elastomer under high-rate loading based on three visco-hyperelastic models: (a) linear viscoelastic model proposed in the present study, (b) YSL2000 model, and (c) SYLL2004 model.

Table 2
Visco-hyperelastic model parameters.

A_1 (MPa)	A_2 (MPa)	A_3 (MPa)	A_4 (MPa)	A_5	G_∞ (MPa)	G_1 (MPa)	θ_1 (μs)
1.107	0.231	0.0344	3.772	3.221	8.308	446.388	1.658

$$\mathbf{s}^{\text{ve}} = \begin{bmatrix} \frac{2}{3}(\lambda - \lambda^{-\mu}) & 0 & 0 \\ 0 & \frac{1}{3}(\lambda^{-\mu} - \lambda) & 0 \\ 0 & 0 & \frac{1}{3}(\lambda^{-\mu} - \lambda) \end{bmatrix} \quad (38)$$

Correspondingly, the strain rate tensor $\overset{.}{\mathbf{s}}^{\text{ve}}$ can be expressed as:

$$\overset{.}{\mathbf{s}}^{\text{ve}} = \begin{bmatrix} \frac{2}{3}\left(1 + \mu\lambda^{-\mu-1}\right)\dot{\lambda} & 0 & 0 \\ 0 & -\frac{1}{3}\left(1 + \mu\lambda^{-\mu-1}\right)\dot{\lambda} & 0 \\ 0 & 0 & -\frac{1}{3}\left(1 + \mu\lambda^{-\mu-1}\right)\dot{\lambda} \end{bmatrix} \quad (39)$$

A combination of Eqs. (33), (36), and (39), together with the uniaxial loading condition ($\sigma_{22} = \sigma_{33} = 0$) and assumption of compressibility ($\mu = 0.485$), yields the Cauchy stress in the loading direction as:

$$\sigma_{11} = \sigma_{11}^{\text{vh}} - \sigma_{22}^{\text{vh}} = \left(\sigma_{11}^{\text{he}} - \sigma_{22}^{\text{he}}\right) + \left(\sigma_{11}^{\text{ve}} - \sigma_{22}^{\text{ve}}\right)$$

$$= 2\left(\frac{A_2}{\lambda^{2.01}} + \frac{A_1 + A_4 e^{-A_5\left(-3 + \frac{2}{\lambda^{0.99}} + \lambda^{1.98}\right)}}{\lambda^{1.02}}\right)\left(-1 + \lambda^{2.97}\right) + \frac{6A_3\left(-\lambda^{3.03} + \lambda^{4.02} + \lambda^{5.01} - \lambda^{6.99} - \lambda^{7.98} + \lambda^{8.97}\right)}{\lambda^{6.03}}$$

$$+ 2G_\infty\left(\lambda - \lambda^{-0.485}\right) + 2G_1 \int_0^t \left(1 + 0.485\lambda^{-1.485}\right)\dot{\lambda}e^{-\frac{t-\tau}{\theta_1}}d\tau \quad (40)$$

where $\lambda(\tau) = \dot{\lambda}\tau + 1$. Note that the model parameters $A_1 \sim A_5$ obtained from step (i) can be directly used in step (ii).

3.3. Model prediction

Following the two-step fitting process, the compressive and tensile responses of polyurea at different strain rates, as described by the model, are plotted in Figs. 10, 11, and the best-fit parameters are listed in Table 2. As shown in Fig. 10a, the quasi-static compressive response is highly nonlinear, exhibiting a sigmoidal profile. As with earlier observations [44], the material exhibits a decreasing rate of hardening ($0.7 < \lambda < 1$), followed by an increasing rate ($0.4 < \lambda < 0.7$). It is noted that the hyperelastic model incorporating an exponential function of I_1 provides a better description of the entire compressive deformation history, especially the sigmoidal profile; in contrast, the model without the exponential term underestimates the true stress at small compressive deformations. In terms of the quasi-static tensile response shown in Fig. 10b, polyurea exhibits high stretchability, with a rupture stretch of ~7, corresponding to an ultimate strength of 150 MPa; this indicates significant potential for blast and impact mitigation applications [64–66]. An effective impact-mitigating elastomeric coating should have both a high strength and ductility [66], because an elastomeric coating with high strength but low ductility will fracture at small strains and spall off, curtailing its contribution to protection [64]. As shown in

Fig. 10b, the proposed model, with or without the exponential term, can describe the concave profile of the experimental response all the way to rupture.

The uniaxial compressive and tensile responses of polyurea at high strain rates are plotted in Fig. 11a. (Note that the positive and negative values of the true stress and stretch rate correspond to tensile and compressive stress states, respectively.) The true stress-stretch response of polyurea is observed to be strongly nonlinear and rate-sensitive. For instance, with an increase in compressive strain rate from 0.001 s^{-1} to 5640 s^{-1}, the compressive stress at $\lambda = 0.6$ increases by five times, from 6 MPa to 30 MPa. There is a similar elevation in the magnitude of tensile stress at a stretch of $\lambda = 1.6$, with an increase in tensile strain rate from 0.001 s^{-1} to 2810 s^{-1}. This rate-dependent response has been attributed to the interaction and readjustment of entangled molecular chains [67]. Fig. 11a shows that the linear viscoelastic model captures both the compressive and tensile stress-stretch responses at high strain rates with acceptable correlation. However, at large compressive deformations (e. g., $\lambda = 0.6$), there is some discrepancy, but this decreases with strain rate.

The linear viscoelastic model proposed is relatively simpler than nonlinear viscoelastic models [40,38,18,39,42,63]. To ascertain the difference caused by employing linear and nonlinear viscoelastic elements, each is adopted in the visco-hyperelastic model illustrated schematically in Fig. 9. Two nonlinear viscoelastic models are considered, and denoted as the YSL2000 model [40] and the SYLL2004 model [38], and the results they yield are shown in Fig. 11b, c (details of these models are presented in the Appendix). It is noted that the model

incorporating a nonlinear viscoelastic element is also able to yield a reasonable description of the dynamic compressive and tensile deformation of polyurea. However, there is an obvious discrepancy with the experimental results for tensile deformation at a stretch rate of $\dot{\lambda} = 1130\text{s}^{-1}$. This may be because the nonlinear models incorporate two terms ($\mathbf{C}$ and $\dot{I}_2$), which are more rate-sensitive to compression than tension [38]. The goodness-of-fit values (R^2) between experimental data and the current model, the YSL2000 model, and the SYLL2004 model, all have the same value of 0.98, indicating negligible difference; i.e., the proposed model is as good as the other two for characterizing the high-rate response of polyurea elastomer. The proposed model is able to describe full recovery of deformation after unloading, but it is noted that accurate and complete capture of viscous dissipation remains to be a challenge, owing to limitations in experimental techniques in eliciting data on the deformation recovery process after high-rate loading.

4. Finite element simulation

The proposed visco-hyperelastic constitutive relationship corresponding to Eq. (33) is implemented in the commercial finite element software Abaqus/Explicit via a user-defined material subroutine (VUMAT); details on how this can be done are described in the "Abaqus User Subroutines Reference Guide v.6.14". A recursive scheme, first proposed by Taylor et al. [68], is employed for calculating the Cauchy
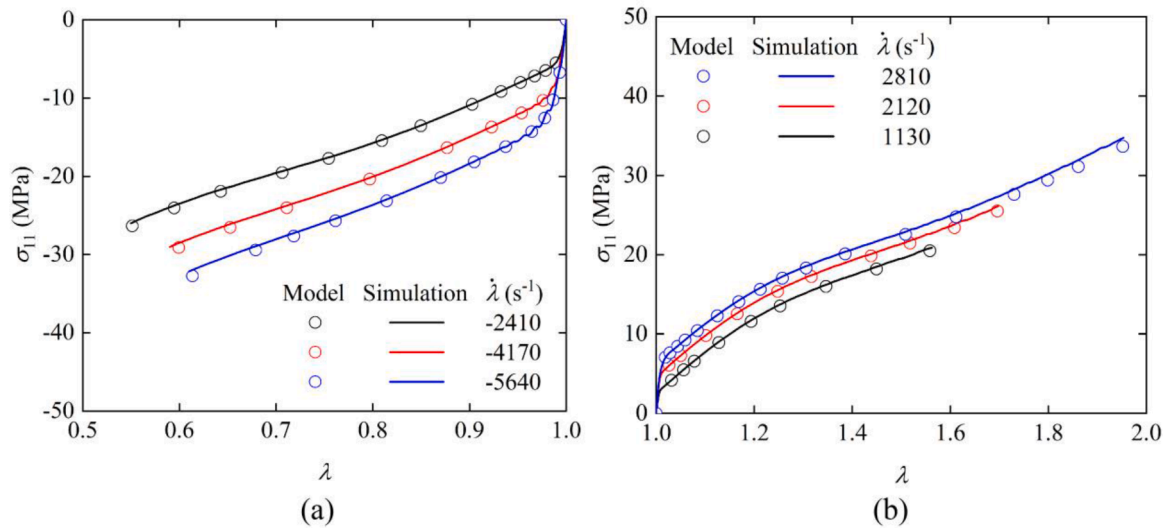
Fig. 12. Comparison between theory and simulation based on eight-element polyurea elastomer block under (a) high-rate compression and (b) high-rate tension.
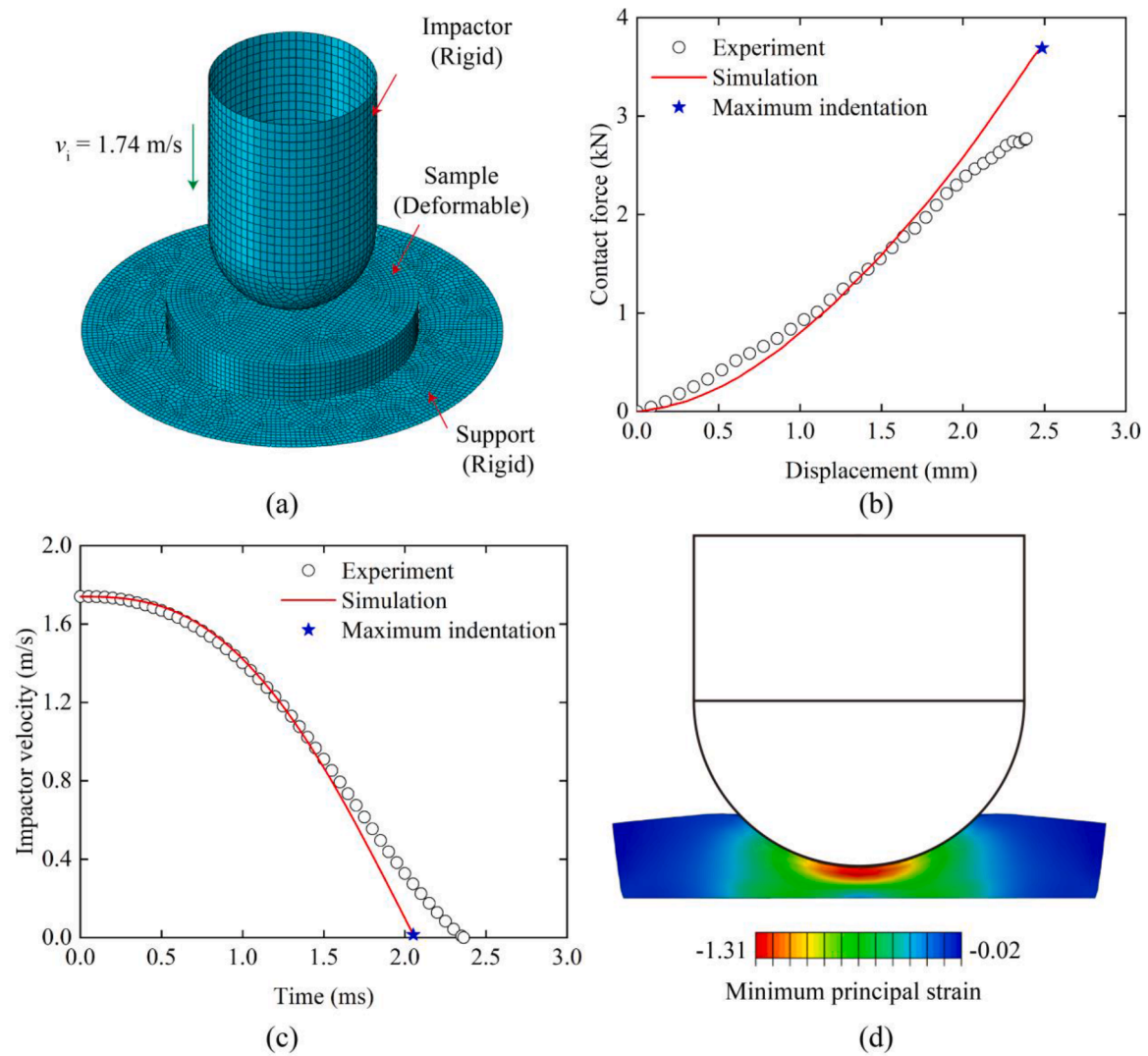

Fig. 13. Simulation of polyurea layer on a rigid base, subjected to drop-weight impact: (a) FE model, (b) variation of contact force with indentation depth, (c) variation of impactor velocity with time, and (d) minimum principal strain contours at maximum indentation.
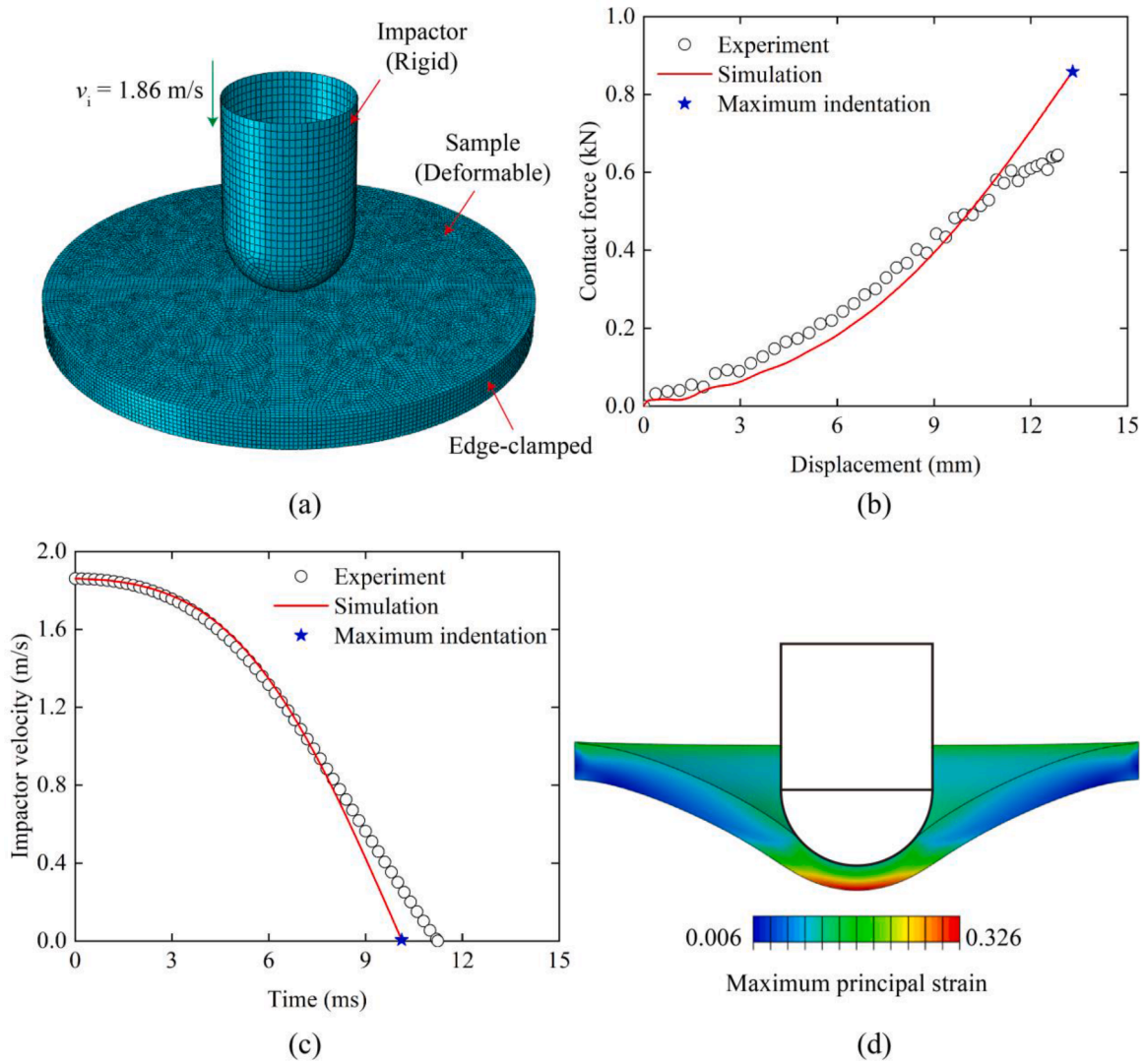
Fig. 14. Simulation of edge-clamped polyurea sheet subjected to drop-weight impact: (a) FE model, (b) variation of contact force with displacement, (c) variation of impactor velocity with time, and (d) maximum principal strain contours corresponding to maximum indentation.

Table 3
Summary of model parameters for other types of polyurea elastomer, for use with proposed constitutive model.

| Test*	Parameters for use with proposed model								Refs.	Year
	A_1(MPa)	A_2(MPa)	A_3(MPa)	A_4(MPa)	A_5(-)	G_∞(MPa)	G_1(MPa)	θ_1(μs)		
T&C	1.126	0.906	−0.0401	5.185	1.659	7.125	206.885	1.609	Yi et al. [37]	2006
									Sarva et al. [44]	2007
									Roland et al. [50]	2007
T&C	2.565	1.465	−0.5707	13.392	16.436	6.003	6685.03	0.142	Leblanc et al. [6]	2015
T&C	2.096	4.121	0.00085	16.493	7.410	14.452	563.535	2.042	Wang et al. [22]	2019
T	−0.036	3.950	0.063	4.371	5.169	4.333	77.182	84.567	Raman et al. [33]	2013
T	12.430	−3.533	−2.294	15.174	5.086	2.628	27.763	552.4	Mohotti et al. [21]	2014
T	−4.684	9.735	0.823	3.444	23.820	17.464	232.029	12.017	Miao et al. [23]	2019
C	8.762	−3.632	0.309	10.009	14.745	4.713	168.279	6.504	Shim and Mohr [72]	2009
C	5.144	−1.158	0.086	4.855	8.227	8.968	657.493	1.822	Liu et al. [73]	2021
C	12.193	−6.396	0.836	2.688	18.987	9.525	74.85	3.173	Gong et al. [71]	2021

*T: tension; C: compression.
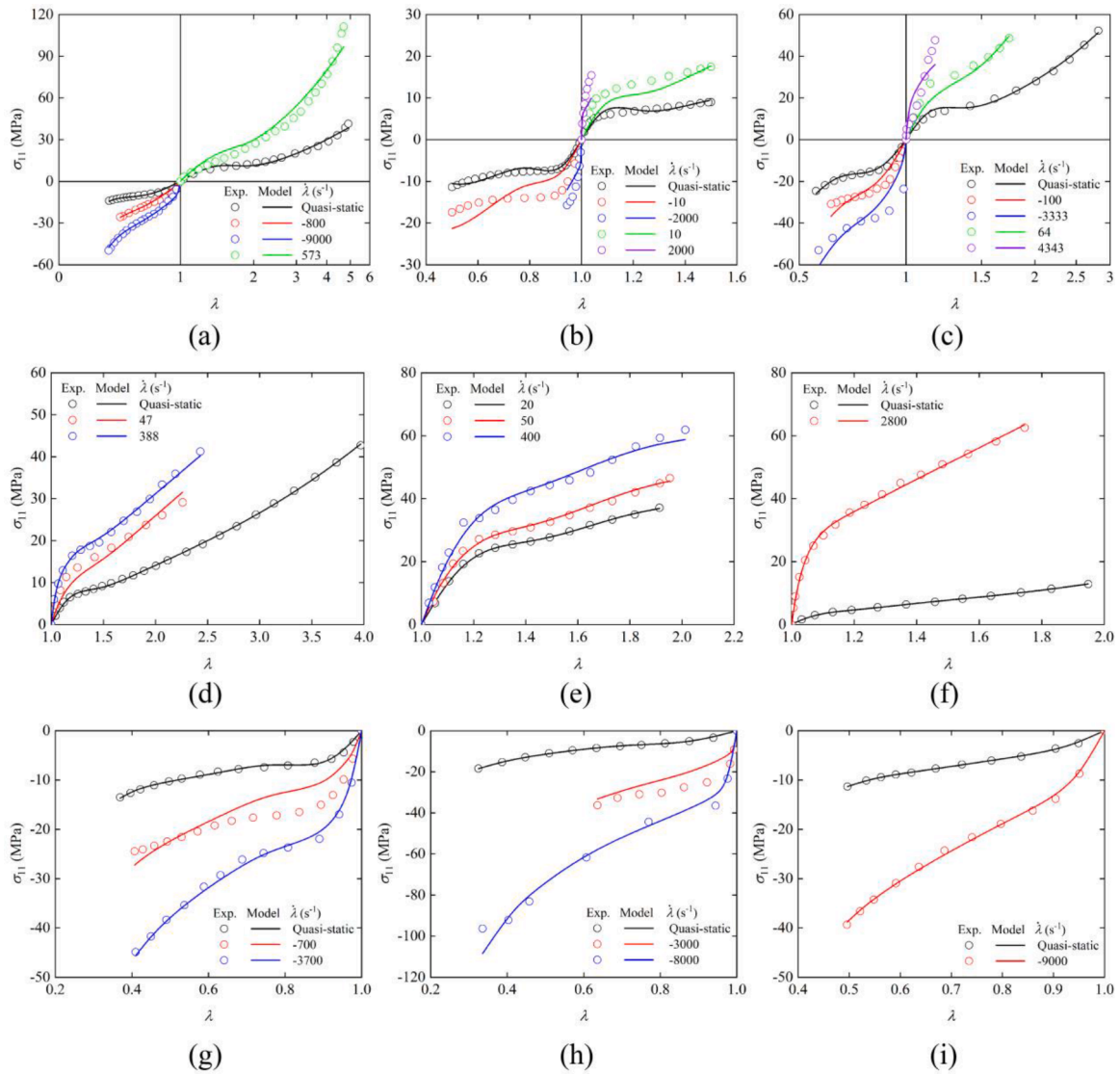
Fig. 15. Comparison of simulation of quasi-static and dynamic compressive and tensile response of polyurea based on proposed model, with published experimental data: (a) Yi et al. [37,44,50], (b) Leblanc and Shukla [6], (c) Wang et al. [22], (d) Raman et al. [33], (e) Mohotti et al. [21], (f) Miao et al. [23], (g) Shim and Mohr [72], (h) Liu et al. [73], and (i) Gong et al. [71].

stress tensor. As previously mentioned, a small degree of compressibility has been introduced into the present model to facilitate numerical computation [69]. With $\mu = 0.485$ selected for the Poisson's ratio, the compressibility parameter D is given by [57]:

$$D = \frac{E}{6(1 - 2\mu)} = \frac{450\text{MPa}}{6(1 - 2 \times 0.485)} = 2.5\text{GPa} \tag{41}$$

where the modulus $E = 450$MPa is an average value determined from the dynamic compressive and tensile curves shown in Fig. 11.

4.1. Results of implementation of constitutive model into FEM simulation

Simulation of two homogenous deformation modes, i.e., uniaxial compression and uniaxial tension, is undertaken to validate appropriate implementation of the constitutive model. A cube with a grid size of 0.5 mm is meshed using eight-node reduced integration (C3D8R) hexahedral elements. A displacement constraint along the loading direction is applied to one side of an eight-element block, and a load is then imposed on the opposite side, resulting in six different constant stretch rates. Conservation of total energy for each simulation is checked. The

material parameters in the numerical simulations are those listed in Table 2. As shown in Fig. 12, for both compressive and tensile deformation at high strain rates, the FE simulation results exhibit good agreement with theoretical predictions.

4.2. Simulation of impact on polyurea layer

To further validate the proposed visco-hyperelastic model, simulation of non-uniform deformation of polyurea subjected to impact by a gravity-driven hemispherically-tipped impactor is carried out. The FE models of the actual tests and the corresponding simulation results are depicted in Figs. 13 and 14. The hemispherical impactor and base support are modeled as rigid bodies and meshed using shell elements, while the polyurea layer is meshed using hexahedral elements. Frictionless surface-surface contact between the impactor and sample is assumed. In accordance with the drop-weight tests described in Section 2.5, two different boundary conditions are imposed on the polyurea, i.e., rigid base-supported (Fig. 13a) and edge-clamped conditions (Fig. 14a). The base-supported layer is fully tied to the rigid support, while all degrees of freedom are constrained at the periphery of the edge-clamped sample (geometric details are presented in Table 1). (Conservation of total

energy in simulations is also checked.)

Figs. 13b and 14b compare experimental observations and numerical simulations in terms of the variation of contact force with impactor displacement. Close agreement is observed for most of the loading history, except for the peak force. The FE simulation captures the maximum indentation but overestimates the peak force. This discrepancy could be attributed to the fact that the sample experiences a wide range of strain rates during loading, and this is difficult to capture completely with a single relaxation time constant in the constitutive model, evaluated solely from experimental data corresponding to high strain rates ($\sim 10^3$ s^{-1}). Omission of the potential effect of adiabatic heating in the current model is also a possible source of discrepancy. Figs. 13c and 14c depict the variation of impactor velocity with time for loading with two different boundary conditions. Evolution of the impactor velocity before the impactor starts to rebound is accurately predicted. Minimum/maximum strain contours for the cross-section of the samples are shown in Figs. 13d and 14d. Localized deformation within the vicinity of contact with the impactor for the base-supported case is compression-dominated, while that for the edge-clamped configuration is tension-dominated. Essentially, this validation of the model with experiments demonstrates that calibration of the model parameters based on uniaxial data provides an adequate description of the dynamic response of polyurea under non-uniform loading conditions.

5. Application of constitutive model

Numerous theoretical, experimental, and numerical efforts devoted to appropriate use of polyurea coating to resist blast and impact have been reviewed [70]. Use of appropriate material models and computational simulation facilitate cost-efficient convergence towards optimal designs. Applicability of the proposed visco-hyperelastic model developed for Qtech-420 polyurea to describe nine other types of polyurea studied [6,21–23,33,37,44,50,71–73] is examined. Their mechanical properties can vary, depending on the fabrication process adopted by suppliers, according to Cui et al. [41]. The polyurea selected are divided into three groups according to the mode of loading, i.e., tension (T), compression (C), and combined tension and compression (T&C). Based on the calibration method described in Section 3.2, the model parameters obtained are listed in Table 3, and a Poisson's ratio of 0.485 is assumed. It may appear unusual that some of the parameters in Table 3 are negative, but this does not violate any fundamental or physical implications [59]. Fig. 15 compares experimental measurements and simulation results based on the proposed model for the nine polyurea materials, and shows that the present model provides reasonable descriptions of the nonlinear variation of true stress with stretch for different strain rates. It is acknowledged that closer correlation may be possible by adopting more complex constitutive models, but a balance between sufficient accuracy and simplicity is the objective.

6. Concluding remarks

This effort focuses on characterizing the dynamic compressive and

tensile properties of a highly stretchable polyurea elastomer (Qtech-420) via a combined experimental, theoretical and numerical approach. Various experiments, which include quasi-static tension/compression tests, SHPB/SHTB dynamic tests, and drop-weight impact tests, are performed. The polyurea material studied is able to elongate by about 700%, and possesses a quasi-static tensile ultimate strength of 150 MPa. Under quasi-static compression, the tangent modulus initially decreases ($0.7 < \lambda < 1$) then increases ($0.4 < \lambda < 0.7$). The compressive and tensile stress-deformation relationships are notably rate-sensitive over the strain rate range from 0.001 s^{-1} to 10^3 s^{-1}. Unlike earlier constitutive models that assume incompressibility, a compressible visco-hyperelastic model is developed to describe the compressive and tensile responses of polyurea at various strain rates. This is based on the addition of rate-independent and rate-dependent Cauchy stress components, involving a five-parameter hyperelastic component and a three-parameter linear viscoelastic component. Good agreement is observed between the model and experimental measurements. Compared with existing models (e.g., the YSL2000 model [40] and the SYLL2004 model [38]), the proposed model yields a closer description of tensile deformation for polyurea at a stretch rate of 10^3 s^{-1}. The model is implemented into a commercial software (Abaqus) via a user-defined material subroutine. Simulations of the impact response of a polyurea sheet by a hemispherically-tipped impactor, which generates non-uniform loading, demonstrate close correlation with experiments. The proposed model is also able to describe the mechanical response of nine other types of polyurea deformed at different strain rates. It is envisaged that the present study will contribute to efficient design and development of blast and impact-resistant polyurea coatings.

CRediT authorship contribution statement

Xin Wang: Conceptualization, Methodology, Software, Writing – original draft, Writing – review & editing. **Haibo Ji:** Investigation, Data curation. **Xue Li:** Investigation, Data curation. **Shengjie Sun:** Investigation. **Qiancheng Zhang:** Methodology. **V.P.W. Shim:** Supervision, Writing – review & editing. **Tian Jian Lu:** Supervision, Funding acquisition, Writing – review & editing.

Declaration of Competing Interest

The authors declare that they have no known competing financial interests or personal relationships that could have appeared to influence the work reported in this paper.

Acknowledgments

Appendix. Brief description of YSL2000 model and SYLL2004 model

The Cauchy stress tensor $\boldsymbol{\sigma}^{\text{ve}}$ for an isotropic, homogenous, and compressible viscoelastic solid can be expressed by:

$$\boldsymbol{\sigma}^{\text{ve}} = \frac{1}{J}\mathbf{F}\cdot\boldsymbol{\Omega}\cdot\mathbf{F}^{\text{T}} \tag{A.1}$$

where $\mathbf{F}$ is the deformation gradient tensor, J is the Jacobian determinant of $\mathbf{F}$ quantifying volumetric change, and $\boldsymbol{\Omega}$ the second Piola-Kirchhoff stress tensor. The form of $\boldsymbol{\Omega}$ governs the stress-deformation relationship and how closely it matches the response of a material.

In the YSL2000 model [40], the second Piola-Kirchhoff stress tensor $\boldsymbol{\Omega}$ is assumed to have the following form:

$$\mathbf{\Omega} = \int_0^t [A_1 + A_2(I_2(\tau) - 3)]\dot{\mathbf{E}}(\tau)e^{\left(-\frac{t-\tau}{A_3}\right)}d\tau \tag{A.2}$$

where A_1, A_2 and A_3 are the model parameters to be determined, I_2 is the second invariant of the right Cauchy-Green deformation tensor $\mathbf{C}$, and $\dot{\mathbf{E}}$ is the Green-St.Venant strain rate tensor.

In the SYLL2004 model [38], the second Piola-Kirchhoff stress tensor $\mathbf{\Omega}$ assumes a different form:

$$\mathbf{\Omega} = (1 + A_1\dot{I}_2(\tau)) \int_0^t \left[A_2\frac{\dot{I}_1(\tau)}{I_1(\tau)}\mathbf{C}(\tau) + 2A_3\dot{\mathbf{E}}(\tau) \right] e^{\left(-\frac{t-\tau}{A_4}\right)}d\tau \tag{A.3}$$

where A_1, A_2, A_3 and A_4 are model parameters to be determined, I_1 is the first invariant of the right Cauchy-Green deformation tensor $\mathbf{C}$, and $\dot{I}_1$, $\dot{I}_2$ are the rates of the first two invariants of $\mathbf{C}$. The two terms $\mathbf{C}$ and $\dot{I}_2$ in the SYLL2004 model result in a higher rate-sensitivity to compressive deformation, to account for a difference in rate-dependence.

Substitution of Eq. (A.2) or (A.3) into Eq. (A.1) yields a three-dimensional frame-independent finite strain viscoelastic model for compressible materials. The model parameters can be determined through a one-dimensional experimental test, as described in Section 3.2. It is noted that only one relaxation time is incorporated into the nonlinear viscoelastic components of the two models.

References

[1] Wang X, He C, Yue Z, Li X, Yu R, Ji H, et al. Shock resistance of elastomer-strengthened metallic corrugated core sandwich panels. Compos Part B Eng 2022: 109840. https://doi.org/10.1016/j.compositesb.2022.109840.

[2] Amini M, Isaacs J, Nemat-Nasser S. Effect of polyurea on the dynamic response of steel plates. In: Proceedings of the SEM Annual Conference and Exposition on Experimental and Applied Mechanics Saint Louis (MO; 2006. p. 1323–6.

[3] Gamache RM, Giller CB, Montella G, Fragiadakis D, Roland CM. Elastomer-metal laminate armor. Mater Des 2016;111:362–8. https://doi.org/10.1016/j.matdes.2016.08.072.

[4] Roland CM, Fragiadakis D, Gamache RM. Elastomer-steel laminate armor. Compos Struct 2010;92:1059–64. https://doi.org/10.1016/j.compstruct.2009.09.057.

[5] Davidson JS, Porter JR, Dinan RJ, Hammons MI, Connell JD. Explosive testing of polymer retrofit masonry walls. J Perform Constr Facil 2004;18:100–6. https://doi.org/10.1061/(ASCE)0887-3828(2004)18:2(100).

[6] Leblanc J, Shukla A. Response of polyurea-coated flat composite plates to underwater explosive loading. J Compos Mater 2015;49:965–80. https://doi.org/10.1177/0021998314528263.

[7] Porter J, Dinan R, Hammons M, Knox K. Polymer coatings increase blast resistance of existing and temporary structures. Amptiac Q 2002;6:47–52.

[8] Primeaux DJ. 100\% solids aliphatic spray polyurea elastomer systems. J Elastomers Plast 1992;24:323–36.

[9] Grujicic M, Yavari R, Snipes JS, Ramaswami S, Runt J, Tarter J, et al. Molecular-level computational investigation of shock-wave mitigation capability of polyurea. J Mater Sci 2012;47:8197–215. https://doi.org/10.1007/s10853-012-6716-4.

[10] Chenwi IN, Ramotowski T, LeBlanc J, Shukla A. Effects of prolonged saline water exposure on the peel strength of polyurea/monel 400 interface. J Adhes 2021;00: 1–17. https://doi.org/10.1080/00218464.2021.1900829.

[11] Ackland K, Anderson C, Ngo TD. Deformation of polyurea-coated steel plates under localised blast loading. Int J Impact Eng 2013;51:13–22. https://doi.org/10.1016/j.ijimpeng.2012.08.005.

[12] Mohotti D, Ngo T, Mendis P, Raman SN. Polyurea coated composite aluminium plates subjected to high velocity projectile impact. Mater Des 2013;52:1–16. https://doi.org/10.1016/j.matdes.2013.05.060.

[13] Amini MR, Simon J, Nemat-Nasser S. Investigation of effect of polyurea on response of steel plates to impulsive loads in direct pressure-pulse experiments. Mech Mater 2010;42:615–27. https://doi.org/10.1016/j.mechmat.2009.09.009.

[14] Amini MR, Isaacs JB, Nemat-Nasser S. Experimental investigation of response of monolithic and bilayer plates to impulsive loads. Int J Impact Eng 2010;37:82–9. https://doi.org/10.1016/j.ijimpeng.2009.04.002.

[15] Li Y, Chen Z, Zhao T, Cao X, Jiang Y, Xiao D, et al. An experimental study on dynamic response of polyurea coated metal plates under intense underwater impulsive loading. Int J Impact Eng 2019;133:103361. https://doi.org/10.1016/j.ijimpeng.2019.103361.

[16] Tekalur SA, Shukla A, Shivakumar K. Blast resistance of polyurea based layered composite materials. Compos Struct 2008;84:271–81. https://doi.org/10.1016/j.compstruct.2007.08.008.

[17] Amirkhizi AV, Isaacs J, McGee J, Nemat-Nasser S. An experimentally-based viscoelastic constitutive model for polyurea, including pressure and temperature effects. Philos Mag 2006;86:5847–66. https://doi.org/10.1080/14786430600833198.

[18] Li C, Lua J. A hyper-viscoelastic constitutive model for polyurea. Mater Lett 2009; 63:877–80. https://doi.org/10.1016/j.matlet.2009.01.055.

[19] Gamonpilas C, McCuiston R. A non-linear viscoelastic material constitutive model for polyurea. Polymer 2012;53:3655–8. https://doi.org/10.1016/j.polymer.2012.06.030 (Guildf).

[20] Shim J, Mohr D. Rate dependent finite strain constitutive model of polyurea. Int J Plast 2011;27:868–86. https://doi.org/10.1016/j.ijplas.2010.10.001.

[21] Mohotti D, Ali M, Ngo T, Lu J, Mendis P. Strain rate dependent constitutive model for predicting the material behaviour of polyurea under high strain rate tensile loading. Mater Des 2014;53:830–7. https://doi.org/10.1016/j.matdes.2013.07.020.

[22] Wang H, Deng X, Wu H, Pi A, Li J, Huang F. Investigating the dynamic mechanical behaviors of polyurea through experimentation and modeling. Def Technol 2019; 15:875–84. https://doi.org/10.1016/j.dt.2019.04.016.

[23] Miao Y, Zhang H, He H, Deng Q. Mechanical behaviors and equivalent configuration of a polyurea under wide strain rate range. Compos Struct 2019;222: 110923. https://doi.org/10.1016/j.compstruct.2019.110923.

[24] Neba Mforsoh I, LeBlanc J, Shukla A. Constitutive compressive behavior of polyurea with exposure to aggressive marine environments. Polym Test 2020;85: 106450. https://doi.org/10.1016/j.polymertesting.2020.106450.

[25] Liu QQ, Wang SP, Lin X, Cui P, Zhang S. Numerical simulation on the anti-penetration performance of polyurea-core Weldox 460 E steel sandwich plates. Compos Struct 2020;236:111852. https://doi.org/10.1016/j.compstruct.2019.111852.

[26] Xue L, Mock W, Belytschko T. Penetration of DH-36 steel plates with and without polyurea coating. Mech Mater 2010;42:981–1003. https://doi.org/10.1016/j.mechmat.2010.08.004.

[27] Chen C, Wang X, Hou H, Cheng Y, Zhang P, Liu J. Effect of strength matching on failure characteristics of polyurea coated thin metal plates under localized air blast loading: experiment and numerical analysis. Thin-Walled Struct 2020;154:106819. https://doi.org/10.1016/j.tws.2020.106819.

[28] Raman SN, Mendis P, Pham T. Elastomeric polymers for retrofitting of reinforced concrete structures against the explosive effects of blast. Adv Mater Sci Eng 2012:2012. https://doi.org/10.1155/2012/754142.

[29] Jiang Y, Zhang B, Wang L, Wei J, Wang W. Dynamic response of polyurea coated thin steel storage tank to long duration blast loadings. Thin-Walled Struct 2021; 163:107747. https://doi.org/10.1016/j.tws.2021.107747.

[30] Jiang Y, Zhang B, Wei J, Wang W. Study on the impact resistance of polyurea-steel composite plates to low velocity impact. Int J Impact Eng 2019;133:103357. https://doi.org/10.1016/j.ijimpeng.2019.103357.

[31] Shi S, Liao Y, Peng X, Liang C, Sun J. Behavior of polyurea-woven glass fiber mesh composite reinforced RC slabs under contact explosion. Int J Impact Eng 2019;132: 103335. https://doi.org/10.1016/j.ijimpeng.2019.103335.

[32] Liao Y, Shi S, Liu Z, Liang C. Study on shock resistance of steel plate reinforced with polyurea–woven fiberglass mesh composite under shock wave. Int J Prot Struct 2018;9:248–66. https://doi.org/10.1177/2041419618755159.

[33] Raman SN, Ngo T, Lu J, Mendis P. Experimental investigation on the tensile behavior of polyurea at high strain rates. Mater Des 2013;50:124–9. https://doi.org/10.1016/j.matdes.2013.02.063.

[34] Mohotti D, Ngo T, Raman SN, Ali M, Mendis P. Plastic deformation of polyurea coated composite aluminium plates subjected to low velocity impact. Mater Des 2014;56:696–713. https://doi.org/10.1016/j.matdes.2013.11.063.

[35] Mohotti D, Ngo T, Raman SN, Mendis P. Analytical and numerical investigation of polyurea layered aluminium plates subjected to high velocity projectile impact. Mater Des 2015;82:1–17. https://doi.org/10.1016/j.matdes.2015.05.036.

[36] El Sayed T, Mock W, Mota A, Fraternali F, Ortiz M. Computational assessment of ballistic impact on a high strength structural steel/polyurea composite plate. Comput Mech 2009;43:525–34. https://doi.org/10.1007/s00466-008-0327-6.

[37] Yi J, Boyce MC, Lee GF, Balizer E. Large deformation rate-dependent stress-strain behavior of polyurea and polyurethanes. Polymer 2006;47:319–29. https://doi.org/10.1016/j.polymer.2005.10.107 (Guildf).

[38] Shim VPW, Yang LM, Lim CT, Law PH. A visco-hyperelastic constitutive model to characterize both tensile and compressive behavior of rubber. J Appl Polym Sci 2004;92:523–31. https://doi.org/10.1002/app.20029.

[39] Pouriayevali H, Guo YB, Shim VPW. A constitutive description of elastomer behaviour at high strain rates - A strain-dependent relaxation time approach. Int J Impact Eng 2012;47:71–8. https://doi.org/10.1016/j.ijimpeng.2012.04.001.

[40] Yang LM, Shim VPW, Lim CT. A visco-hyperelastic approach to modelling the constitutive behaviour of rubber. Int J Impact Eng 2000;24:545–60. https://doi.org/10.1016/S0734-743X(99)00044-5.

[41] Cui J, Shi Y, Zhang X, Huang W, Ma M. Experimental study on the tension and puncture behavior of spray polyurea at high strain rates. Polym Test 2021;93: 106863. https://doi.org/10.1016/j.polymertesting.2020.106863.

[42] Guo H, Guo W, Amirkhizi AV. Constitutive modeling of the tensile and compressive deformation behavior of polyurea over a wide range of strain rates. Constr Build Mater 2017;150:851–9. https://doi.org/10.1016/j.conbuildmat.2017.06.055.

[43] Rusty GT, Iii G, Blumenthal WR. Split-hopkinson pressure bar testing of soft materials. Mech Test Eval 2018;8:488–96. https://doi.org/10.31399/asm.hb.v08.a0003298.

[44] Sarva SS, Deschanel S, Boyce MC, Chen W. Stress-strain behavior of a polyurea and a polyurethane from low to high strain rates. Polymer 2007;48:2208–13. https://doi.org/10.1016/j.polymer.2007.02.058 (Guildf).

[45] Kolsky H. An investigation of the mechanical properties of materials at very high rates of loading. Proc Phys Soc Sect B 1949;62:676.

[46] Gerlach R, Kettenbeil C, Petrinic N. A new tensile bar design. Int J Impact Eng 2012;50:63–7. https://doi.org/10.1016/j.ijimpeng.2012.08.004.

[47] Pouriayevali H, Guo YB, Shim VPW. A visco-hyperelastic constitutive description of elastomer behaviour at high strain rates. Procedia Eng 2011;10:2274–9. https://doi.org/10.1016/j.proeng.2011.04.376.

[48] Sharma A, Shukla A, Prosser RA. Mechanical characterization of soft materials using high speed photography and split hopkinson pressure bar technique. J Mater Sci 2002;37:1005–17. https://doi.org/10.1023/A:1014308216966.

[49] Chen W, Lu F, Cheng M. Tension & compression tests under quasi-static & dynamic loading. Polym Test 2002;21:113–21.

[50] Roland CM, Twigg JN, Vu Y, Mott PH. High strain rate mechanical behavior of polyurea. Polymer 2007;48:574–8. https://doi.org/10.1016/j.polymer.2006.11.051 (Guildf).

[51] Green MS, Tobolsky AV. A new approach to the theory of relaxing polymeric media. J Chem Phys 1946;14:80–92. https://doi.org/10.1063/1.1724109.

[52] Bergström J. Mechanics of solid polymers: theory and computational modeling. 2015. https://doi.org/10.1016/C2013-0-15493-1.

[53] Wang X, Huang X, Gao M, Zhao Y. Mechanical response of kerogen at high strain rates. Int J Impact Eng 2021;155:103905. https://doi.org/10.1016/j.ijimpeng.2021.103905.

[54] Boyce MC, Arruda EM. Constitutive models of rubber elasticity: a review. Rubber Chem Technol 2000;73:504–23. https://doi.org/10.5254/1.3547602.

[55] Rivlin RS. Large elastic deformations of isotropic materials IV. Further developments of the general theory. Philos Trans R Soc London Ser A, Math Phys Sci 1948;241:379–97.

[56] Bischoff JE, Arruda EM, Grosh K. A new constitutive model for the compressibility of elastomers at finite deformations. Rubber Chem Technol 2001;74:541–59. https://doi.org/10.5254/1.3544956.

[57] Hohenberger TW, Windslow RJ, Pugno NM, Busfield JJC. A constitutive model for both low and high strain nonlinearities in highly filled elastomers and

[58] Yeoh OH. Characterization of elastic properties of carbon-black-filled rubber vulcanizates. Rubber Chem Technol 1990;63:792–805. https://doi.org/10.5254/1.3538289.

[59] Yeoh OH. Some forms of the strain energy function for rubber. Rubber Chem Technol 1993;66:754–71. https://doi.org/10.5254/1.3538343.

[60] Gent AN. A new constitutive relation for rubber. Rubber Chem Technol 1996;69: 59–61.

[61] Coleman BD, Noll W. Foundations of linear viscoelasticity. Rev Mod Phys 1964;36: 1103. https://doi.org/10.1103/RevModPhys.36.1103.2.

[62] Ferry JD. Viscoelastic properties of polymers. John Wiley & Sons; 1980.

[63] Khajehsaeid H, Arghavani J, Naghdabadi R, Sohrabpour S. A visco-hyperelastic constitutive model for rubber-like materials: a rate-dependent relaxation time scheme. Int J Eng Sci 2014;79:44–58. https://doi.org/10.1016/j.ijengsci.2014.03.001.

[64] Xue Z, Hutchinson JW. Neck retardation and enhanced energy absorption in metal-elastomer bilayers. Mech Mater 2007;39:473–87. https://doi.org/10.1016/j.mechmat.2006.08.002.

[65] Xue Z, Hutchinson JW. Neck development in metal/elastomer bilayers under dynamic stretchings. Int J Solids Struct 2008;45:3769–78. https://doi.org/10.1016/j.ijsolstr.2007.10.006.

[66] McShane GJ, Stewart C, Aronson MT, Wadley HNG, Fleck NA, Deshpande VS. Dynamic rupture of polymer-metal bilayer plates. Int J Solids Struct 2008;45: 4407–26. https://doi.org/10.1016/j.ijsolstr.2008.03.017.

[67] Bergström JS, Boyce MC. Constitutive modeling of the large strain time-dependent behavior of elastomers. J Mech Phys Solids 1998;46:931–54. https://doi.org/10.1016/S0022-5096(97)00075-6.

[68] Taylor RL, Pister KS, Goudreau GL. Thermomechanical analysis of viscoelastic solids. Int J Numer Methods Eng 1970;2:45–59.

[69] Fallon C, McShane GJ. Fluid-structure interactions for the air blast loading of elastomer-coated concrete. Int J Solids Struct 2019;168:138–52. https://doi.org/10.1016/j.ijsolstr.2019.03.017.

[70] Iqbal N, Tripathi M, Parthasarathy S, Kumar D, Roy PK. Polyurea coatings for enhanced blast-mitigation: a review. RSC Adv 2016;6:109706–17. https://doi.org/10.1039/c6ra23866a.

[71] Gong C, Chen Y, Li T, Liu Z, Zhuang Z, Guo B, et al. Free volume based nonlinear viscoelastic model for polyurea over a wide range of strain rates and temperatures. Mech Mater 2021;152:103650. https://doi.org/10.1016/j.mechmat.2020.103650.

[72] Shim J, Mohr D. Using split Hopkinson pressure bars to perform large strain compression tests on polyurea at low, intermediate and high strain rates. Int J Impact Eng 2009;36:1116–27. https://doi.org/10.1016/j.ijimpeng.2008.12.010.

[73] Liu Q, Chen P, Guo Y, Su J, Han L, Arab A, et al. Mechanical behavior and failure mechanism of polyurea nanocomposites under quasi-static and dynamic compressive loading. Def Technol 2021;17:495–504. https://doi.org/10.1016/j.dt.2020.02.006.

implementation with user-defined material subroutines in abaqus. Rubber Chem Technol 2019;92:653–86. https://doi.org/10.5254/RCT.19.80387.